Journal of Colloid and Interface Science 709 (2026) 139972

Contents lists available at ScienceDirect

Journal of Colloid And Interface Science

journal homepage: www.elsevier.com/locate/jcis

Biomimetic lipid nanoparticles for RNA delivery to breast cancer microenvironment cells by enhanced homotypic and heterotypic adhesion

Stefania Garbujo [a,b,1], Chiara Baioni [a,1], Andrea Banfi [a], Leonardo Bolis [a], Giulia Bonvini [a], Elena Del Favero [c], Paola Gagni [d], Alessandro Gori [d], Linda Barbieri [a,b], Marco Davide Giustra [a,b], Giulia Tomaino [a], Lucia Morelli [a,b], Clizia Chinello [e], Fulvio Magni [e], Lucia Salvioni [a,b,*], Miriam Colombo [a,b,*], Davide Prosperi [a,b,*]

[a] Department of Biotechnology and Bioscience, University of Milano-Bicocca, Piazza della Scienza 2, 20126 Milano, Italy
[b] Nanomedicine Center NANOMIB, University of Milan-Bicocca, Milan, Italy
[c] Department of Medical Biotechnology and Translational Medicine, University of Milano, Viale Fratelli Cervi 93, 20054 Segrate, MI, Italy
[d] National Research Council of Italy-Istituto di Scienze e Tecnologie Chimiche (SCITEC-CNR); Via M. Bianco 9, 20131, Milano, Italy
[e] Department of Medicine and Surgery, Proteomics and Metabolomics Unit, University of Milano-Bicocca, via Podgora 23, Vedano al Lambro, 20854, MB, Italy

HIGHLIGHTS

- Biomimetic lipid nanoparticles camouflaged with cancer cell membrane nanoghosts were developed for targeted RNA delivery.
- Nanoghost coating preserved homotypic and heterotypic recognition proteins, enabling targeting and efficient RNA delivery.
- BLNPs showed high affinity for cancer-associated fibroblasts, while uncoated LNPs had minimal stromal cell interaction.
- SAXS and physicochemical analyses confirmed BLNPs as stable core-shell hybrids preserving the multilamellar LNP structure.

GRAPHICAL ABSTRACT

SAXS and physicochemical analyses confirmed BLNPs as stable core-shell hybrids preserving the multilamellar LNP structure.

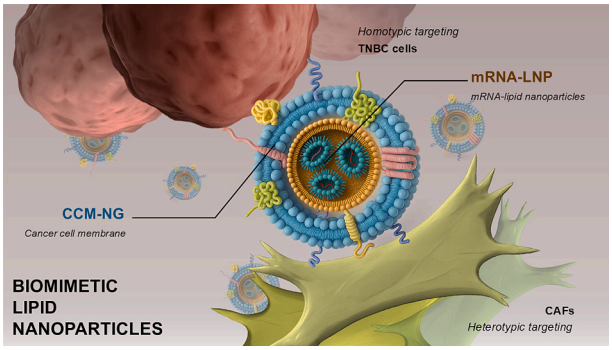

ARTICLE INFO

Keywords:
Biomimetic synthesis
Lipid nanoparticles
RNA delivery
Camouflaging nanoparticles
Heterotypic targeting

ABSTRACT

Lipid nanoparticles (LNPs) have emerged as a clinically validated nonviral RNA delivery system. However, their limited tumor targeting remains challenging in oncology. In this work, LNPs were functionally integrated with cancer cell membrane components to enhance their targeting capabilities. The natural composition of tumor membranes was leveraged to promote both homotypic and heterotypic adhesion, exploiting cancer cell self-recognition and interactions with stromal cells in the tumor microenvironment. A biomimetic nanocarrier was developed by cloaking RNA-loaded LNPs with nanoghosts obtained from the membrane of triple negative breast cancer cells. Nanoghosts were dye-labeled and comprehensively characterized in terms of size, surface charge, protein composition, and membrane sidedness. The functional orientation of nanoghost membrane-associated

* Corresponding authors at: Department of Biotechnology and Bioscience, University of Milano-Bicocca, Piazza della Scienza 2, 20126 Milano, Italy.
E-mail addresses: lucia.salvioni@unimib.it (L. Salvioni), miriam.colombo@unimib.it (M. Colombo), davide.prosperi@unimib.it (D. Prosperi).
[1] Stefania Garbujo and Chiara Baioni contributed equally to this work.

https://doi.org/10.1016/j.jcis.2026.139972
Received 26 October 2025; Received in revised form 21 January 2026; Accepted 23 January 2026
Available online 24 January 2026

proteins mediated homotypic binding with 4 T1 cells and heterotypic recognition of functionally validated cancer-associated fibroblasts and exhibited higher affinity for the latter, as confirmed through flow cytometry and confocal microscopy. RNA-LNPs were incorporated into nanoghosts using ultrasound-assisted fusion, yielding stable biomimetic LNPs with a multilamellar mRNA-LNP core enveloped by a nanoghost shell, as confirmed by Small-Angle X-ray Scattering. While uncoated LNPs showed negligible interaction with heterotypic cells, biomimetic LNPs displayed strong affinity for cancer-associated fibroblasts, enabling efficient internalization and RNA transfection. Additionally, the biomimetic coating enhanced LNP uptake in homotypic 4 T1 cells, resulting in significantly improved biological activity compared to uncoated LNPs. This work provides proof of concept that RNA-LNPs can be effectively integrated into biomimetic carriers to enable dual targeting of tumor and stromal cells. The enhanced selectivity and delivery performance of biomimetic LNPs highlight their therapeutic potential for overcoming stromal barriers in desmoplastic tumors such as triple negative breast cancer.

1. Introduction

The advances in gene therapy in cancer treatment rely not only on a good molecular strategy but also on the need for safe, efficient, and target-selective delivery systems [1,2]. Direct in vivo administration of naked RNA is unstable and immunogenic, thus requiresing the use of a suitable delivery system to protect the RNA from nucleases and to enhance transfection efficiency [3].

After the Covid-19 pandemic, nanomedicine and RNA gene therapy have been broadly recognized, considering that over 75% of the world population has received RNA vaccines as of August 2025 [4]. Hence, the development of nonviral RNA delivery vectors has become an area of active research. The delivery systems most widely explored to date include lipid carriers, polymers, and encoded protein derivatives [5–7]. Compared to other nonviral nanocarriers, the use of lipid nanoparticles (LNPs) is an established technology, and most mRNA therapeutics already approved or under development rely on LNPs [8]. LNPs are generally composed of a mixture of an ionizable lipid, a zwitterionic phospholipid, cholesterol, and a lipid-poly(ethylene glycol) (PEG) conjugate. Ionizable lipids are cationic at low pH (enabling RNA complexation) and neutral at physiological pH (reducing potential toxic effects of positively charged lipids). Depending on their size and physicochemical properties, LNPs are generally taken up by cells via energy-dependent endocytosis, and lipid ionizability is thought to enable endosomal escape during endosome maturation, thus releasing the cargo into the cytoplasm [9].

While a clinical benefit has been achieved with Covid vaccination, LNPs still suffer from poor efficacy in the delivery of gene therapeutics in oncology. The main reasons for this limitation reside in the poor bioavailability and low colloidal stability during blood circulation, and in the lack of tumor selectivity, which is a prerequisite for effective cancer therapy [10]. So far, the application of intravenously administered RNA-LNPs has been limited to hepatocarcinoma, achieving only poorly specific cell distribution within the liver [8,11–13].

Coating the nanoparticles with entire cancer cell membranes or with their components provides them with various cell-like biological properties, including immune escape, prolonged systemic circulation and cell-cell recognition in the tumor microenvironment (TME) [14]. This top-down approach takes advantage of cancer cell membrane derived nanovesicles, also termed nanoghosts (CCM-NGs), to camouflage nanoparticles as “self” and impart them long circulation in plasma preventing the recognition by the reticuloendothelial system [15]. In addition, CCM-NGs bestow nanoparticles with inherent properties of the source cell membranes and are therefore widely investigated for tumor homing, exploiting the homotypic self-recognition of cancer cells [16,17].

Despite the obvious advantages offered by improved targeting and prolonged preservation in the blood, to our knowledge the successful camouflaging of RNA-LNPs with CCM-NGs has not been demonstrated. In this work, we propose a reliable method for the preparation of biomimetic LNPs (BLNPs) designed for tumor homing and characterize their structural and functional properties. To this aim, RNA-LNPs obtained by microfluidic technology were integrated with CCM-NGs. The natural composition of tumor cell membranes was investigated to achieve not only homotypic but also heterotypic targeting, taking advantage of the intrinsic interaction of cancer cells with the TME. CCM-NGs were produced from isolated membranes and carefully characterized, identifying a set of ligands involved in adhesion processes potentially fostering TME tropism and those conferring stealth properties to the nanocarrier.

Among the various types of solid tumors, triple-negative breast cancer (TNBC) represents a paradigmatic model of desmoplastic malignancy, characterized by an abundant fibrotic stroma that contributes to therapeutic resistance and impaired intratumor drug delivery [18,19]. Cancer cells are poorly accessible within the dense stromal barrier. Thus, we aimed to develop a delivery platform capable of targeting the abundant and easily reachable cellular populations with the TME. In this context, cancer-associated fibroblasts (CAFs) have emerged as an attractive target for TME remodulation and gene therapy, given their pivotal role in desmoplasia and their perivascular localization [20]. Therefore, the TNBC model was selected both for its clinical relevance and for its prominent desmoplastic features and associated delivery challenges. A representative CAF model compatible with the murine 4 T1 breast cancer cells was derived from the commercially available NIH3T3 fibroblast cell line, using a recently validated protocol (manuscript in preparation). This approach allowed us to explore both homotypic (tumor-to-tumor) and heterotypic (tumor-to-CAF) interactions, providing a comprehensive assessment of the BLNP delivery system within a representative TME model system.

2. Methods

2.1. Materials

Mammalian cell culture media and supplements, including DMEM, RPMI-1640, fetal bovine serum (FBS), calf bovine serum (CBS), penicillin–streptomycin, L-glutamine, PBS, and trypsin-EDTA, were purchased from Euroclone (Italy) and used as supplied. Analytical-grade mannitol (CAS 69–65-8), sucrose (CAS 57–50-1), Tris-HCl (CAS 77–86-1), HEPES (CAS 7365-45-9), EDTA (CAS 6381-92-6), and imidazole (CAS 288–32-4) were purchased from Sigma-Aldrich (Merk, Germany). Triton X-100 (molecular-biology grade; CAS 9002-93-1), Tween-20 (molecular-biology grade; CAS 9005-64-5) agarose (molecular-biology grade; CAS 9012-36-6), and sodium citrate dihydrate (≥ 99%; CAS 6132-04-3;) were also obtained from Sigma-Aldrich (Merck, Germany). Glycine (≥ 99%; CAS 56–40-6), phenylmethylsulfonyl fluoride (PMSF; ≥ 98.5%; CAS 329–98-6) and bovine serum albumin (BSA; ≥ 98%; CAS 9048-46-8) were used as supplied. Protease inhibitor cocktail (Thermo Fisher Scientific, USA; cat. no. 78438), recombinant Proteinase K (Ambion, USA; cat. no. AM2546; DNase/RNase-free; ≥600 U/mL), and recombinant human TGF-β1 (>98% by SDS-PAGE/HPLC; endotoxin <1 EU/μg; Abcam, UK; cat. no. ab50036) were used at molecular-biology grade. SYBR™ Safe DNA Gel Stain (Thermo Fisher Scientific, USA; cat. no. S33102) and TrackIt™ Cyan/Orange Loading Buffer (Thermo Fisher Scientific, USA; cat. no. 10482035) were used for DNA gel electrophoresis. For bead-based orientation assays, an anti-mouse/human CD44

monoclonal antibody (BioLegend, USA; cat. no. 318; unconjugated) and a rat IgG$_2$B isotype control (R&D Systems, USA; cat. no. MAB0061; Protein A/G-purified; unconjugated) were used together with aldehyde/sulfate latex beads (Invitrogen/Thermo Fisher Scientific, USA; cat. no. A37304). For immunofluorescence, a rat anti-mouse CD44 monoclonal antibody (clone IM7; Bio-Rad, USA; cat. no. MCA4703; purified IgG) was used together with an Alexa Fluor™ Plus 555-conjugated goat anti-rat IgG (H + L) secondary antibody (Thermo Fisher Scientific, USA; cat. no. A48263; affinity-purified). Hoechst 33342 (≥99% purity by HPLC; Thermo Fisher Scientific, USA; cat. no. 62249) was used as supplied. For western blotting, primary antibodies against Na^+/K^+ ATPase (Abcam, UK; cat. no. ab76020), GAPDH (Abcam, UK; cat. no. ab8245), calnexin (Abcam, UK; cat. no. ab22595), CD324/*E*-Cadherin (clone DECMA-1; Thermo Fisher Scientific, eBioscience™, USA; cat. no. 14–3249-82), and CD47 (Abcam, UK; cat. no. ab218810) were used together with HRP-conjugated secondary antibodies goat anti-rabbit IgG (Cell Signaling Technology, USA; cat. no. 7074S), goat anti-mouse IgG (Cell Signaling Technology, USA; cat. no. 7076), and goat anti-rat IgG (Abcam, UK; cat. no. ab97057). ECL Star Enhanced Chemiluminescent Substrate (≥99%; Euroclone, Italy; cat. no. EMP001005) was used as supplied. Protein concentrations were determined using a bicinchoninic acid (BCA) protein assay kit (Cyanagen, Italy; cat. no. PRTD1,0500) according to the manufacturer's instructions. For SiMoA assays, a biotin-conjugated anti-mouse CD44 monoclonal antibody (clone KM81; Invitrogen, USA; cat. no. MA517869; Protein G-purified) was employed. Bead Wash Buffer, Bead Block Buffer, Bead Diluent, Homebrew Sample Diluent, and SBG (Quanterix, USA; code 101351), as well as SBG-enzyme, SBG Diluent, and RPG substrate (Quanterix, USA; code 101361), were used as supplied. EDC (1-ethyl-3-(3-dimethylaminopropyl)carbodiimide hydrochloride; Thermo Fisher Scientific, USA; Pierce™ EDC No-Weigh™ Format; cat. no. 77149) was used in high-purity crystalline form. The MSP peptide used in SiMoA assays was synthesized using a previously published procedure [21]. After automated SPPS synthesis, the peptide was purified by RP-HPLC to >95% purity, pooled, lyophilized, and stored at −20 °C. Annexin-V-PE (BioLegend, USA; cat. no. 640947; affinity-purified; low-endotoxin formulation), CellTrace™ Far Red Proliferation Kit (Thermo Fisher Scientific, USA; cat. no. C34564; high-purity amine-reactive dye; ≥95% by HPLC), and paraformaldehyde (Sigma-Aldrich, Merck, Germany; CAS 30525–89-4; 95%) were used as supplied. Lipids for LNP synthesis included DSPC (Avanti Polar Lipids, USA; cat. no. 850365P), DMG-PEG (Avanti Polar Lipids, USA; cat. no. 880151P), SM-102 (MedChemExpress, USA; cat. no. HY-134541), and cholesterol (Avanti Polar Lipids, USA; cat. no. 700000P), all used as supplied. Absolute ethanol (HPLC grade; Sigma-Aldrich, Merck, Germany) was used for lipid dissolution. CleanCap® mCherry mRNA (Cy5-UTP/5moU; 1 mg; TriLink BioTechnologies, USA; cat. no. WOTL123905) was used as supplied. Lipophilic dyes DiO (Invitrogen, USA; cat. no. D275; molecular-biology grade) and DiD (Invitrogen, USA; cat. no. D7757; molecular-biology grade), as well as uranyl acetate (Electron Microscopy Sciences, USA; electron-microscopy grade), were used as supplied. For quantitative proteomic analysis, peptides were prepared using the iST 96× Sample Preparation Kit (PreOmics, Germany) according to the manufacturer's instructions. LC-MS-grade solvents, including acetonitrile (ACN; ≥99.9%), formic acid (≥99%), and water, were purchased from Sigma-Aldrich (Merck, Germany). MMI-L Tuning Mix (Agilent Technologies, USA) was used for mass-spectrometer calibration. Evotip Pure™ trap columns and PepSep C18 analytical columns (Evosep Biosystems, Denmark) were used as supplied. All reagents were used without further purification.

2.2. Cell cultures

NIH3T3 mouse embryonic fibroblasts (ATCC® CRL-1658™) were cultured in Dulbecco's Modified Eagle Medium (DMEM, Euroclone) supplemented with 10% calf bovine serum (CBS, Euroclone), 1% penicillin-streptomycin and 1% L-glutamine (Euroclone). 4 T1 mouse mammary carcinoma cells (AMSBio, iCell-m067) were cultured in Roswell Park Memorial Institute (RPMI) 1640 medium (Euroclone) supplemented with 10% fetal bovine serum (FBS, Euroclone), 1% penicillin-streptomycin, and 1% L-glutamine. For CAF-like induction, NIH3T3 cells were first allowed to adhere in standard culture conditions. The medium was then replaced with DMEM containing 1% CBS and 5 ng/mL TGF-β (Abcam), and cells were incubated for 16 h to promote CAF-like differentiation. All cells were maintained at 37 °C in a humidified incubator with 5% and passaged prior to confluence. Cells were regularly tested for mycoplasma, and all experiments were performed on mycoplasma-free cells.

2.3. Isolation of 4 T1 cancer cell membranes and CCM-NGs production

4 T1 cells were cultured in T-175 flasks (Corning) until reaching full confluency. After two washes with Ca^{2+}/Mg^{2+}-free PBS (pH 7.4), cells were detached using trypsin-EDTA and pelleted by centrifugation. The cell pellet was resuspended in 0.3 mL of homogenization buffer composed of 225 mM mannitol, 75 mM sucrose, 0.1 mM EDTA, 30 mM Tris-HCl (pH 7.4), and a protease inhibitor cocktail (Halt™ Protease Inhibitor Cocktail, 100×). Cell disruption was performed using a motor-driven homogenizer (DWK Life Sciences) operating at 2,000 rpm with a polypropylene pestle for 1 min on at 4 °C. The resulting homogenate was centrifuged at 1,000 ×*g* for 5 min to remove intact cells and debris; this step was repeated five times to ensure complete homogenization. The post-nuclear supernatant was subsequently centrifuged at 7,000 ×*g* for 10 min to pellet crude mitochondria. The remaining supernatant was then subjected to ultracentrifugation at 100,000 ×*g* for 45 min (Beckman SW 41 Ti rotor, Beckman Coulter) to isolate the total membrane fraction. The final cytosolic supernatant was separately collected for WB analysis. The membrane pellet was resuspended in sucrose buffer (0.25 mM sucrose, 10 mM HEPES, pH 7.4, 1 mM EDTA, and protease inhibitors), followed by a second ultracentrifugation at 100,000 ×*g* for 45 min to further purify the membrane fraction. The final pellet was resuspended in 0.2 mL of sucrose buffer, briefly sonicated for 10 s using a water-bath sonicator (Branson Ultrasonics 5510), and stored at 4 °C. CCM-NGs were generated via membrane extrusion. The membrane suspension was diluted in 1 mL sucrose buffer and sequentially extruded through 800 nm and 400 nm polycarbonate membranes (10 passes each; Avanti Polar Lipids) using a mini extruder (Avanti Polar Lipids). CCM-NGs were stored ad 4 °C.

2.4. Plasma membrane isolation via density gradient centrifugation

A total membrane fraction was isolated from 4 T1 cells using the protocol described in the above section, yielding a mixture likely comprising plasma membrane along with endoplasmic reticulum (ER) and Golgi membranes. The possibility of improving plasma membrane purity was explored as a potential approach using density gradient centrifugation. While this method resulted in superior enrichment of the plasma membrane fraction, the total membrane fraction was ultimately preferred for downstream applications due to its higher yield and procedural simplicity. For density gradient centrifugation, the cell membrane pellet obtained from the total membrane isolation was resuspended in 4 mL of 1.4 M sucrose prepared in 10 mM HEPES and 1 mM EDTA (pH 7.4). A discontinuous sucrose gradient was then assembled in 13.2 mL Ultra-Clear thin-wall ultracentrifuge tubes (Beckman Coulter) by sequentially layering 1 mL of 2.0 M sucrose, 2 mL of 1.6 M sucrose, the 4 mL of membrane suspension, 3 mL of 1.2 M sucrose, and 2 mL of 0.8 M sucrose, all prepared in 10 mM HEPES and 1 mM EDTA (pH 7.4). Samples were centrifuged at 28,500 rpm for 2.5 h at 4 °C using a SW41 Ti rotor (Beckman Coulter). Following centrifugation, three discrete bands were observed and collected separately (Fig. S4a). Each fraction was diluted with buffer containing 25 mM imidazole and 1 mM EDTA (pH 7.4), and subjected to ultracentrifugation at 100,000 ×*g* for

30 min at 4 °C. The resulting pellets were resuspended in 0.2 mL of sucrose buffer (composition as above) and stored at 4 °C.

2.5. Labeling of CCM-NGs with lipophilic dyes

CCM-NGs were fluorescently labeled using carbocyanine-based lipophilic dyes. Among the reported strategies for nanovesicle labeling, carbocyanine dyes were selected due to their low fluorescence in aqueous environments and strong membrane-associated signal, enabling efficient membrane labeling. Conventional post-production labeling resulted in the formation of dye micelles with dimensions comparable to CCM-NGs, complicating purification. To overcome this, a pre-labeling strategy was adopted: 4 T1 cells were stained prior to membrane isolation and CCM-NG production (Fig. S11). This approach enabled effective integration of fluorophores into the vesicle membrane. Two dyes were employed: DiO (3,3′-dioctadecyloxacarbocyanine perchlorate), characterized by a high extinction coefficient, and DiD (1,1′-dioctadecyl-3,3,3′,3′-tetramethylindodicarbocyanine-4-chlorobenzene sulfonate), which exhibits red-shifted excitation/emission spectra suitable for imaging in autofluorescent backgrounds. For optimization of labeling conditions with both dyes, 4 T1 cells were seeded in 12-well plates at a density of 60,000 cells/mL in 1 mL of complete growth medium and cultured at 37 °C. After 24 h the medium was removed, cells were washed twice with PBS without Ca^{2+} and Mg^{2+} and incubated with 0.5 mL of serum-free medium containing either DiO [(3,3′-Dioctadecyloxacarbocyanine Perchlorate), Invitrogen] or DiD [(1,1′-Dioctadecyl-3,3,3′,3′-Tetramethylindodicarbocyanine, 4-Chlorobenzenesulfonate Salt), Invitrogen] at final concentrations of 1, 5, or 10 μM. After 2 h incubation, cells were detached using trypsin-EDTA, centrifuged at 200 ×*g*, resuspended in PBS containing 1% EDTA and analyzed by flow cytometry (Fig. S12). Fluorescence intensity was analyzed using a Gallios Flow Cytometer (Beckman Coulter Inc.). For DiO-labeled cells, excitation was performed at 448 nm and emission was collected using a 525/40 nm band-pass filter. For DiD-labeled cells, excitation was performed at 638 nm and emission was collected using a 660/20 nm band-pass filter. Data analysis was performed using Kaluza software (Beckman Coulter Inc.). The labeling condition that provided the highest fluorescent signal was selected for the preparation of CCM-NGs, following the same protocol described in the previous section (*Isolation of 4 T1 cell membranes and CCM-NGs production)*. As shown in Fig. S13, the retention of the orange (DiO) and blue (DiD) colour was observed throughout the membrane isolation process. After production, DiO- and DiD-labeled CCM-NGs were characterized; both formulations exhibited size distribution and surface charge comparable to their unlabeled counterparts (Fig. S14a), indicating that dye incorporation did not affect the physicochemical properties of the vesicles. Fluorometric analysis confirmed the characteristic emission spectra of each fluorophore (Fig. S14c). Furthermore, Western blot analysis demonstrated the presence of the membrane marker Na^+/K^+ ATPase in both labeled CCM-NG formulations (Fig. S14b), confirming successful retention of membrane protein during processing.

2.6. Physicochemical and morphological characterization of nanoparticles

The hydrodynamic size (reported as *Z*-average, i.e., cumulants mean) and Z-potential (as an indicator of surface charge) of the nanoparticles were measured using a Zetasizer UltraRed (Malvern Instruments Ltd., Worcestershire, UK) equipped with a 633 nm laser and a fixed backscatter detection angle of 173°. Samples were diluted in phosphate-buffered saline (PBS) to maintain attenuator values between 7 and 9, ensuring optimal signal intensity. Measurements were performed at room temperature, and results are reported as mean ± standard deviation (SD) from three independent replicates. Size distribution and particles concentration were further assessed by nanoparticles tracking analysis (NTA) using an NTA Pro system (Malvern Instruments Ltd.) equipped with 488 nm laser. Samples were prepared by dilution in PBS previously filtered through 0.02 μm polyethersulfone (PES) syringe filters. For each sample, five independent 60 s videos acquisitions were recorded, and data were analyzed using the integrated NTA software. Data are reported as raw measurements and expressed as mean ± SD. Nanoparticles morphology was examined by transmission electron microscopy (TEM) using a Tecnai G2 Spirit BioTWIN microscope (FEI) operating at 120 kV. Samples were diluted in ultrapure water and deposited onto 200-mesh copper grids coated with Formvar (Ted Pella, CA, USA). After 1 min, excess liquid was removed by blotting, and the grids were negatively stained with 2% uranyl acetate (prepared as 1% in PBS, pH 7.5). Grids were air-dried prior to imaging.

2.7. Immunoblot analysis of CCM-NGs

Western blotting was performed to assess the presence of compartment-specific protein markers in cytosolic and CCM-NG fractions. Samples were lysed using RIPA buffer, and total protein concentration was determined using the bicinchoninic acid (BCA) assay. Equal amounts of protein (1.5 μg per lane) were separated on a NuPAGE™ 4–12% Bis-Tris polyacrylamide gel (Invitrogen) and subsequently transferred onto a polyvinylidene difluoride (PVDF) membrane. Membranes were blocked for 1 h at room temperature in Tris-buffered saline (TBS) containing 5% bovine serum albumin (BSA) and 0.1% Tween-20. Antibody incubation was performed overnight at 4 °C using the following antibodies: anti-Na^+/K^+ ATPase, anti-Calnexin, anti-GAPDH, anti-CD324, and anti-CD47. After three washes with phosphate-buffered saline (PBS) containing 0.1% Tween-20, membranes were incubated for 2 h at room temperature with HRP-conjugated secondary antibodies: anti-rabbit IgG, anti-mouse IgG, and anti-rat IgG. Signal detection was carried out using ECL Star chemiluminescent reagent, and images were acquired with the Odyssey Imaging System (LI-COR Biosciences). Densitometric analysis of protein bands was performed using Fiji (ImageJ) software.

2.8. Characterization of membrane fractions isolated by density gradient centrifugation

The three distinct membrane fractions obtained by density gradient centrifugation were characterized for their protein content via Western blot analysis (Fig. S4b,c). Calnexin was selected as a marker for the endoplasmic reticulum (ER), while Na^+/K^+-ATPase and GAPDH were used as biomarkers for the plasma membrane and cytosol, respectively. Densitometric analysis revealed a significant difference in GAPDH content between the cytosolic fraction and the three membrane fractions, confirming effective separation of membrane-bound components. Among the gradient-separated fractions, the band corresponding to the 1.0 M sucrose density region (fraction 1) exhibited the highest enrichment in the plasma membrane marker (Na^+/K^+ ATPase) and the lowest enrichment in the ER marker (Calnexin) compared to fractions 2 and 3 (Fig. 28b). These findings support the identification of fraction 1 as the plasma membrane fraction, in agreement with literature reports [22]. Fractions 2 and 3 were consequently attributed to the ER and Lysosomes/Golgi membranes, respectively. Notably, the presence of Calnexin in the plasma membrane fraction can be rationalized by previous findings demonstrating that Calnexin may be partially translocated to the cell surface, where it plays a functional role as a chaperone. Further characterization of the three membrane fractions was performed by dynamic light scattering (DLS) and zeta potential (*Z*-potential) measurements (Fig. S5). DLS analysis revealed an average particle size of approximately 240 nm for fractions 1 and 2, and about 290 nm for fraction 3. In contrast, all three fractions exhibited similar Z-potential values, ranging from −26.3 mV to −31.5 mV, indicating comparable surface charge characteristics. Due to the limited sample availability, the fractions were not extruded as performed for the total membrane fraction. Instead, bath sonication was employed as an alternative

downsizing method, relying on ultrasonic energy to disrupt the lipid bilayer and facilitate reassembly into smaller vesicles.

Collectively, these results demonstrate that density gradient centrifugation offers superior plasma membrane enrichment compared to differential centrifugation. However, due to its relatively low yield and labor-intensive nature, the total membrane fraction was selected for subsequent production of cell-derived membrane nanovesicles (CCM-NGs).

2.9. Fluorometric analysis of labeled-CCM-NGs.

luorescence spectra of labeled CCM-NGs were acquired using a Fluoromax-4P spectrofluorimeter (Horiba Scientific, NJ, USA). DiO-labeled CCM-NGs were excited at 488 nm, and emission spectra were recorded from 500 to 600 nm. For DiD-labeled CCM-NGs, excitation was performed at 637 nm, with emission spectra collected between 650 and 750 nm. All samples were appropriately diluted in PBS prior to measurements.

2.10. Quantitative proteomic analysis of CCM-NGs

(1) Kit-Assisted Trypsination. Six independent CCM-NG preparations (F1-F6) were processed using the iST 96× sample preparation kit (PreOmics, In-StageTip Sample Preparation), with minor adaptations and tube-compatible adapters. Briefly, 50 µg of protein extract were mixed with an equal volume of 2× lysis buffer. The mixture was incubated at 95 °C for 10 min with continuous shaking (1000 rpm), followed by ten cycles of 30-s ON/OFF sonication. After denaturation and solubilization, enzymatic digestion was initiated by adding the digestion buffer provided in the kit, and samples were incubated at 37 °C for 3 h. The reaction was then stopped by the addition of the STOP solution. Peptides were transferred to the cartridge system included in the kit and purified by centrifugation at 3800 x*g* for 2 min. The clean-up procedure included two wash steps and two elution steps using the corresponding reagents provided. The eluates were dried in a HETOVAC vacuum concentrator (Savant) and resuspended in LC-LOAD buffer to a final concentration of 1 µg μL^{-1}. Prior to LC-MS analysis, samples were gently shaken (500 rpm, 5 min). Peptide concentration was determined using a NanoDrop OneC spectrophotometer (Thermo Scientific, Wilmington, DE, USA).

(2) DIA PASEF Acquisition Workflow for Deep Proteomics. For each sample, 400 ng of peptides were injected in triplicate into an Evosep One liquid chromatography system (Evosep Biosystems, Odense, Denmark), coupled online to a timsTOF fleX™ mass spectrometer (Bruker Daltonics, Bremen, Germany), as previously described with slight modifications [23]. Peptides were first loaded onto Evotip Pure™ trap columns (Evosep Biosystems) according to the manufacturer's instructions, then separated on a PepSep C18 analytical column (8 cm length, 1.5 µm particle size, 150 µm internal diameter) maintained at 40 °C. Chromatographic separation was performed using a 21-min gradient (60 samples per day, SPD) with mobile phase A (0.1% formic acid in water) and mobile phase B (acetonitrile with 0.1% formic acid). Eluted peptides were ionized using a nanoBooster CaptiveSpray™ source (Bruker Daltonics). The mass spectrometer operated in Data-Independent Acquisition (DIA) mode combined with Parallel Accumulation-Serial Fragmentation (PASEF). MS data were acquired in positive ion mode over an *m/z* range of 100–1700 and an ion mobility range of 0.80–1.30 V·s/cm^2. Dry gas flow was set to 3.0 L min^{-1} at 180 °C, with a capillary voltage of 1700 V. To reduce MS2 spectral complexity, singly charged ions were excluded from PASEF-DIA tandem MS acquisition. Data were collected across a mass range of 348.1–973.1 Da and an ion mobility range of 0.80–1.22 1/K0, with 10 PASEF cycles per run and 25 Da isolation windows, resulting in a total cycle time of approximately 1.17 s. Mass accuracy was ensured through calibration using a low-concentration tuning mix (MMI-L, Agilent Technologies, Santa Clara, CA, USA). Mass and ion mobility calibration were performed using three lock masses (*m/z* 622.0290, 922.0098, and 1221.9906) applied via a lock mass filter.

(3) Data Elaboration. Library-Free Processing and Quantification. Raw MS data were processed using Spectronaut™ software (version 18.1, Biognosys, https://biognosys.com) through a library-free approach. The identification was performed against the *Mus musculus* reference proteome (SwissProt, downloaded on May 12, 2023; 17,155 entries). Search parameters included trypsin as the digestion enzyme, carbamidomethylation of cysteines as a fixed modification, and oxidation of methionine and N-terminal protein acetylation as variable modifications. The false discovery rate (FDR) was controlled at 1% at both the precursor and protein levels. Protein abundance values were automatically cross-run normalized by the software. Proteins were considered confidently identified only if supported by at least one unique and significant peptide.

(4) Proteomic data analysis. Proteins identified in >50% of all runs were considered reproducibly detected. For downstream analysis, proteins were filtered by excluding those with a coefficient of variation (CV%) greater than 30%, incomplete sequence coverage across all batches, and abundance values below 100. Subcellular localization was assessed for the top 148 most abundant proteins (relative abundance >1000), uniProt annotations for *Mus musculus*. Gene Ontology Cellular Component (GO:CC) enrichment analysis was performed on the full set of 998-high confidence proteins using Enrichr (https://maayanlab.cloud/Enrichr/enrich) and the Compartments Curated (2025) database. Clustergram visualization of top GO:CC terms and representative proteins was generated to highlight compartmental overlap and functional enrichment. GO term association were mapped onto the quantitative dataset, and cumulative relative abundance of proteins associated with GO:CC terms related to cell junction (GO:0030054) (e.g., focal adhesion, cell-substrate junction) was calculated as a percentage of the total protein abundance.

2.11. Validation of CCM-NG membrane protein orientation

Aldehyde/sulfate latex beads (4 µm; Invitrogen, Life Technologies) were functionalized with either anti-CD44 antibody (BioLegend) or IgG_2B isotype control antibody (R&D Systems). Briefly, 5 µL of beads (~6×10^6 beads) were incubated overnight at room temperature with 25 µg of antibody diluted in 0.5 mL of PBS. Following incubation, beads were centrifuged at 3,000 ×*g* for 3 min, and the pellet was washed three times with 0.5 mL of 0.5% BSA in PBS (PBS-BSA). Beads were then treated with 50 µL of 1 M glycine for 30 min at room temperature to quench unreacted aldehyde groups, followed by three additional PBS-BSA washes. For binding assays, functionalized beads were incubated with 5 µg (based on protein content) of DiO-labeled CCM-NGs (in 0.1 mL of PBS-BSA 0.5%) for 2 h at room temperature under gentle agitation. As controls, beads were also incubated with unlabeled CCM-NGs or with DiO-labeled CCM-NGs pre-digested with Proteinase K (for 1 h at 37 °C). After incubation, all samples were centrifuged at 3,000 ×*g* for 3 min and washed three times with PBS-BSA before analysis. DiO fluorescence in beads population was assessed by flow cytometry using a CytoFLEX S instrument (Beckman Coulter), and data were analyzed with CytExpert software.

2.12. Membrane sensing peptides (MSP) based SiMoA assays

Following the manufacturer's protocol, 2.8 × 10^9 particles/mL of carboxylated paramagnetic beads from the Quanterix Homebrew SiMoA

kit were activated using EDC. Subsequently, 300 μL of a 1 mM NH_2-PEG_4-N_3 solution (Sigma-Aldrich) in PBS was added, and the mixture was shaken for 2 h. After two washes with Bead Wash Buffer (Quanterix) to remove unreacted components, the beads were incubated with 300 μL of 100 μM MSP-DBCO in PBS for 1 h under continuous mixing. Post-conjugation, the beads were washed twice, blocked with Bead Block Buffer (Quanterix) for 15 min at room temperature with shaking, and washed again. The functionalized beads were stored in Bead Diluent (Quanterix) at 4 °C until use. CCM-NGs were diluted 1:5000 in Homebrew Sample Diluent (Quanterix). A total of 100 μL of each diluted sample was added in duplicate to a 96-well microplate, followed by the addition of 25 μL of MSP-conjugated beads to each well. The mixture was incubated for 2 h shaking at 800 rpm. After incubation, beads were washed using an automated plate washer and then incubated for 10 min with anti-CD44-biotin monoclonal antibody (Invitrogen). Following another wash, beads were incubated for 10 min with 100 μL of SBG in SBG Diluent (Quanterix). After a final wash, the plate and RGP substrate (Quanterix) were loaded into the Quanterix SR-X instrument for automated detection and quantification.

2.13. Cellular uptake of dye-labeled CCM-NGs by flow cytometry and fluorescence microscopy

The uptake of DiO- and DiD-labeled CCM-NGs by CAFs and 4 T1 cells was assessed by flow cytometry. For CAF experiments, NIH3T3 cells were seeded in 24-well plates (Costar, Corning) at a density of 20,000 cells/well. After cell adhesion, the medium was replaced with 0.5 mL of medium containing 1% calf bovine serum and 5 ng/mL TGF-β, and cells were incubated for an additional 12 h at 37 °C to induce CAF-like differentiation. Cells were then treated DiO- or DiD-labeled CCM-NGs (20 μg mL^{-1}, based on protein content; 0.5 mL/well) for 1, 2, 4, or 6 h in complete medium. Following incubation, cells were washed twice with PBS (without Ca^{2+} and Mg^{2+}), detached using trypsin-EDTA and analyzed using a CytoFLEX flow cytometer (Beckman Coulter). DiO fluorescence was excited at 488 nm and detected using a 525/40 nm band-pass filter, while DiD was excited at 638 nm and detected using a 660/20 nm band-pass filter. For each condition, 10,000 single-cell events were recorded. For 4 T1 uptake experiments, cells were seeded in 24-well plates at a density of 35,000 cells/well and cultured for 24 h in complete medium. Cells were then incubated with DiO- or DiD-labeled CCM-NGs (20 μg mL^{-1}) following the same protocol described above. For fluorescence microscopy, NIH3T3 cells were seeded in glass-bottom culture dishes (Greiner Bio-one) at a density of 40,000 cells/well and cultured for 24 h. Following CAF differentiation, cells were incubated for 1 h with 0.5 mL of complete medium containing DiO- or DiD-labeled CCM-NGs (20 μg mL^{-1}). After incubation, cells were washed with cold PBS fixed with 4% paraformaldehyde (0.3 mL/well, 20 min, room temperature). Cells were then rinsed with PBS, blocked with 2% BSA in PBS (0.5 mL/well, 30 min, room temperature), and stained with a primary anti-CD44 antibody (BioRad) followed by a goat anti-rat AlexaFluor plus 555 secondary antibody (Thermo Fisher). Nuclei were counterstained with Hoechst (0.2 mL/well, 5 min, room temperature), and cells were washed with PBS. Images were acquired using a Leica Thunder Imager (Leica Microsystems, USA) equipped with a 63× objective.

2.14. CCM-NGs uptake in CAF/4 T1 co-culture model

Uptake of DiO-labeled CCM-NGs was evaluated using a co-culture model comprising CAFs and 4 T1 cells. Following CAF differentiations, cells were detached and labeled with CellTrace™ Far Red Cell Proliferation Kit (5 μM) for 30 min at 37 °C, to enable their discrimination from 4 T1 cells during flow cytometry analysis. CAFs and 4 T1 cells were then co-seeded in 12-well plates at an equal density of 35,000 cells/well to ensure comparable cell numbers at the time of nanoparticle exposure. 16 h after seeding, cells were treated with DiO-labeled CCM-NGs at a final concentration of 20 μg mL^{-1} (based on protein content) for 10, 20 30, 40 min. Unlabeled CCM-NGs were used as negative control. Incubation was carried out under both endocytosis-permissive (37 °C) and endocytosis-inhibitory (4 °C) conditions. For experiments at 4 °C, following nanoparticle exposure, cells were washed twice with PBS and subsequently incubated at 37 °C for 1 h to allow internalization. Cells were then detached, washed, and labeled with Annexin-V-PE (Biolegend) for 15 min at room temperature to discriminate viable cells. Samples were subsequently analyzed by flow cytometry using a CytoFLEX flow cytometer (Beckman Coulter). Cellular uptake was detected in DiO channel after acquisition of 10,000 single cells per sample. The gating strategy and representative dot plots for 37 °C and 4 °C conditions are shown in Fig. S16 and S17, respectively.

2.15. Proteinase K digestion assay

DiD-labeled CCM-NGs were subjected to enzymatic digestion by incubation with Proteinase K (PK, 100 μg mL^{-1}) for 1 h at room temperature (+ PK). Following digestion, PK was inactivated by the addition of phenylmethylsulfonyl fluoride (PMSF, final concentration 1 mM) for 5 min at room temperature. Control samples (untreated CCM-NGs, (−PK) were processed under identical conditions using Proteinase K buffer alone. After completion of the digestion protocol, CCM-NGs were resuspended in complete cell medium at a final concentration of 20 μg mL^{-1} (protein content). Nanoparticles uptake (1 h incubation) was evaluated in target cells using fluorescence microscopy or flow cytometry as described in the section "*Cellular uptake of dye-labeled CCM-NGs by flow cytometry and fluorescence microscopy*". CCM-NGs incubation was carried out under both endocytosis-permissive (37 °C) and endocytosis-inhibitory (4 °C) conditions. For experiments at 4 °C, following nanoparticle exposure, cells were washed twice with PBS and subsequently incubated at 37 °C for 1 h to allow internalization. The same digestion protocol was applied for co-culture experiments, in which DiO-labeled CCM-NGs were used in place of DiD-labeled CCM-NGs.

2.16. BLNPs synthesis

Lipid nanoparticles (LNPs) encapsulating Cy5-labeled mCherry mRNA were formulated using distearoylphosphatidylcholine (DSPC), cholesterol, 1,2-dimyristoyl-rac-glycerol-3-methoxypolyethylene glycol-2000 (DMG-PEG), and the ionizable lipid SM-102. Lipids were dissolved in ethanol at a molar ratio of 51:10:38.5:0.5 (SM-102:DSPC: cholesterol: DMG-PEG) and mixed with Cy5-labeled mCherry mRNA (TriLink BioTechnologies) in 25 mM citrate buffer (pH 4.0) at a nitrogen-to-phosphate (N/P) ratio of 6:1. The aqueous and organic phases were combined at a flow rate ratio (FRR) of 3:1 (aqueous: ethanol) using a Sunshine microfluidic mixing system (Unchained Labs) at a total flow rate (TFR) of 12 mL min^{-1}. The resulting LNP suspension was dialyzed against phosphate-buffered saline (PBS, pH 7.4) for 16 h at 4 °C to remove residual ethanol. For the preparation of biomimetic LNPs (BLNPs), DiO-labeled CCM-NGs were mixed with Cy5-mCherry LNPs at a protein-to-mRNA ratio of 12, defined as the ratio between the micrograms of total protein content in CCM-NGs and the micrograms of encapsulated mRNA in LNPs. The mixture was sonicated in a water bath sonicator (Branson, 42 kHz) at RT for 2 min. After production, BLNPs were stored at 4 °C until further use.

2.17. RNA encapsulation quantification

RNA encapsulation efficiency in LNPs was determined using the Quant-iT™ RiboGreen® RNA Assay Kit (Life Technologies) according to manufacturer's instructions with minor modifications. LNPs samples (1.65 μL) were diluted in TE buffer (10 mM Tris-HCl, 20 mM EDTA, Thermo Scientific), either in the presence or absence of 0.5% (*v*/v) Triton X-100 (Sigma-Aldrich). Samples containing Triton X-100 were incubated at 37 °C for 15 min to release encapsulated RNA. Standard

curves were generated by serial dilutions of mCherry mRNA in TE buffer with and without 0,5% Triton X-100. Aliquots of samples and standards (in triplicates) were loaded into black 96-well plates, and Ribogreen reagent was added. Fluorescence was measured using a microplate reader (Ensight, PerkinElmer) at 485 nm excitation and 528 nm emission. Encapsulation efficiency (EE%) was calculated using the following equation:

$$EE\% = [(\text{Total RNA} - \text{Unencapsulated RNA}) / \text{Total RNA}] \times 100.$$

Total RNA was determined from the fluorescence of Triton-treated LNPs, while unencapsulated RNA was obtained from untreated samples.

Notably, this assay could not be applied to BLNP owing to the strong interference caused by cell membrane components.

2.18. SAXS characterization

Small Angle X-ray experiments were carried out at the ID02 high-brilliance beamline at ESRF (Grenoble, Fr), experiment MD-1456 [24]. 50 μL of each sample were inserted in a flow-through cell, a quartz capillary 2 mm thick, allowing for the measurement of buffers and samples in the same configuration. Two different sample-to detector distances (1 and 10 m) were chosen to acquire the scattered intensity in a wide range of the momentum transfer $q = 4\pi\sin(\theta/2)/\lambda$, being θ the scattering angle and $\lambda = 0.1$ nm the radiation wavelength. All measurements were performed at room temperature. Twenty short frames (0.1 s) were acquired and averaged, after check of no radiation damage. The 2D patterns were normalized and azimuthally averaged to obtain the 1D I(q) profiles, that represent the excess scattered intensity of nanoparticles, after subtraction of empty cell and buffer contributions. Analysis of the SAXS profiles was performed by SasView software tool [www.sasview.org].

2.19. Agarose gel electrophoresis

Agarose gels (1.5% *w/v*) were prepared in 1× Tris-borate-EDTA (TBE) buffer. After cooling, SYBR™ Safe DNA Gel Stain was added, and the solution was gently mixed before casting. For mRNA encapsulation analysis, LNPs were incubated with 0.5% (*v*/v) Triton X-100 at 65 °C for 10 min and vortexed. Untreated LNPs (w/o Triton) were used for comparison. LNPs-Triton, LNPs w/o Triton and free mRNA, were mixed with TrackIt™ Cyan/Orange Loading Buffer, loaded in the gel (0.7 μg mRNA per lane) and electrophoresed at 110 V for 20 min in 1× TBE buffer. Gels were imaged using a LI-COR Odyssey imaging system (LI-COR Biosciences). For BLNPs characterization, uncoated LNPs were sonicated in a water bath sonicator (Branson 2510, 42 kHz) at room temperature for 2 min. Afterward, sonicated LNPs, together with untreated LNPs and BLNPs were processed as described above.

2.20. Cell viability assay

Cell viability was assessed using the MTS assay (CellTiter 96® AQueous One Solution Cell Proliferation Assay, Promega) according to the manufacturer's instructions. 4 T1 cancer cells and CAFs were seeded in 96-well plates at a density of 1×10^4 cells/well and incubated for 24 h at 37 °C in a humidified atmosphere with 5% CO_2. Cells were then treated with LNPs, CCM-NGs, or BLNPs (1.5 μg mL^{-1}, based of mRNA content) and incubated for 24, 48, and 72 h. At each time point, 20 μL of MTS reagent was added to each well and incubated for 2 h at 37 °C. Absorbance was measured at 490 nm using a microplate reader. Cell viability was calculated as a percentage relative to untreated control cells.

2.21. BLNPs uptake in CAFs

CAFs obtained as previously described were seeded in glass-bottom culture dishes (Greiner Bio-One) at a density of 40,000 cells/well. After adhesion, cells were incubated for 1 h with 0.5 mL of complete medium containing the following formulations: DiO-labeled CCM-NGs, Cy5-LNPs, BLNPs, or a physical mixture of CCM-NGs and LNPs (1.5 μg mL^{-1}, based on mRNA content). For the CCM-NGs group, an amount equivalent to that used in the BLNPs and physical mix formulations was employed. All samples were tested either with or without Proteinase K pre-treatment (as previously described). After incubation, cells were washed with cold PBS and fixed with 4% paraformaldehyde (0.3 mL/well, 20 min, room temperature). Samples were then rinsed with PBS, blocked with 2% BSA in PBS (0.5 mL/well, 30 min, room temperature), and stained with a primary anti-CD44 antibody (Bio-Rad), followed by a goat anti-rat Alexa Fluor Plus 555-conjugated secondary antibody. Nuclei were counterstained with Hoechst 33342 (0.2 mL/well, 5 min, room temperature), and cells were washed thoroughly with PBS. Fluorescence images were acquired using a Leica Thunder Imager (Leica Microsystems, USA) equipped with a 63× objective. Colocalization between LNPs (Cy5 fluorescence) and CCM-NGs (DiO fluorescence) was analyzed by calculating Manders' colocalization coefficients using ImageJ software.

2.22. BLNPs transfection in CAFs and 4 T1 cancer cells

4 T1 cells and CAFs (obtained as previously described) were seeded in 48-well plates at a density of 15.000 cells/well. After 24 h growth, cells were treated with BLNPs and uncoated LNPs (1.5 μg mL^{-1}, based of mRNA content) in complete medium. 24, 48, and 72 h after treatment, cells were detached and mCherry expression was assessed by flow cytometry as previously described.

3. Results and discussion

3.1. Production and morphological characterization of CCM-NGs

An optimized multistep process was established to produce CCM-NGs, involving large-scale expansion and digestion of parental TNBC cells, membrane isolation, and formation of uniform nanoscale vesicles. TNBC cells were lysed under hypotonic conditions to induce swelling, rupture, and release of cytoplasmic contents (Fig. S1 and S2 in SI). The resultant membrane fragments were purified and processed via mechanical extrusion to form nanosized vesicles. Comprehensive physicochemical characterization of CCM-NGs was performed to assess size distribution, surface charge, and morphology. Dynamic light scattering (DLS) measurements revealed a substantial size reduction after extrusion, from 333 to 157 nm, accompanied by a marked decrease in polydispersity index (PDI) from 0.6 to 0.16, indicating of a more uniform vesicle population (Fig. 1a). Zeta potential analysis confirmed a net negative surface charge for both pre- and post-extrusion samples (−21 and − 26 mV, respectively), consistent with the anionic character of phospholipid bilayers (Fig. 1b). Morphological analysis by transmission electron microscopy (TEM) confirmed the structural refinement achieved through extrusion (Fig. S3). Pre-extrusion vesicles exhibited heterogeneous and irregular shapes, whereas post-extrusion CCM-NGs displayed well-defined, cup-shaped nanostructures reminiscent of naturally occurring exosomes (Fig. 1c).

Despite the slight improvement in membrane purity, additional purification by density gradient centrifugation significantly reduced yield and offered no functional advantages for CCM-NGs (details in Methods section, Figs. S4, S5).

To evaluate the reproducibility of CCM-NG fabrication process, six independent batches (F1-F6) were prepared and characterized for their physicochemical properties. Despite being produced manually, all batches displayed excellent consistency, with non-significant differences in size, PDI and surface charge (Fig. S6). In addition, all samples exhibited remarkable colloidal stability, retaining their physicochemical integrity over a 28-day storage, with no significant changes in hydrodynamic size, PDI or zeta potential (Fig. S7). These results demonstrate the robustness and scalability of the CCM-NGs production workflow.

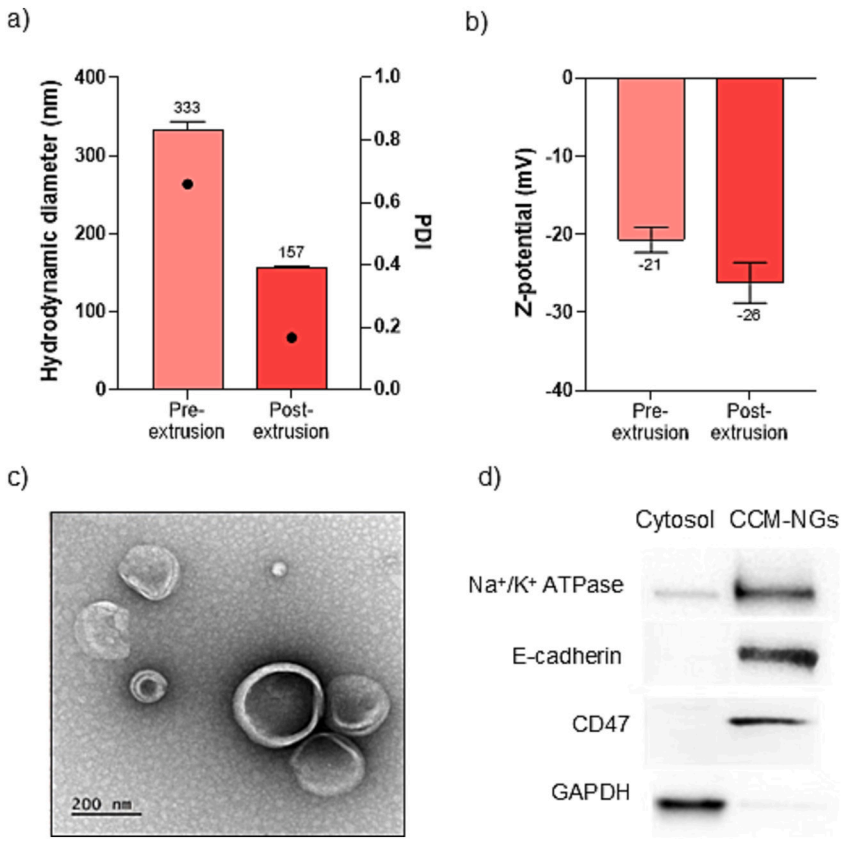

Fig. 1. Physicochemical characterization of CCM-NGs: (a) Hydrodynamic diameter and PDI of samples before and after extrusion, measured by DLS; (b) Zeta potential analysis of pre- and post-extrusion samples. Data are presented as mean ± SD ($n = 3$ independent measurements); (c) TEM image of extruded CCM-NGs (scale bar: 200 nm); (d) Biochemical characterization of CCM-NGs by immunoblotting. Cytosolic fraction and CCM-NGs were probed with antibodies against plasma membrane-specific markers, including Na^+/K^+ ATPase, E-cadherin, CD47, and cytosol marker glyceraldehyde 3-phosphate dehydrogenase (GAPDH).

3.2. Biochemical profiling of CCM-NGs

A key feature of CCM-NGs is their ability to retain the molecular complexity of the parental cancer cell membrane including its lipid composition and membrane protein repertoire. In particular, the preservation of cell adhesion molecules is critical, as these proteins mediate homotypic interaction and multicellular aggregation among cancer cells [25].

To evaluate the protein content of CCM-NGs, western blot analysis was performed on fractions collected at different stages of differential centrifugation, including unbroken cells, cytosolic extract, and membrane-enriched fraction. This analysis aimed to assess the enrichment of proteins specific to distinct cellular compartments. Sodium-potassium ATPase (Na^+/K^+ ATPase) was selected as a plasma membrane marker due to its constitutive expression and its role in mediating homotypic cancer cell targeting [26]. Glyceraldehyde-3-phosphate dehydrogenase (GAPDH) was used as a cytosolic marker.

To compare the relative abundance of these markers, equal total protein amounts were loaded across lanes representing 4 T1 cells, cytosol fraction, pre-extrusion membranes, and post-extrusion CCM-NGs. Na^+/K^+ ATPase was highly enriched in the membrane fraction prior to extrusion, with minimal GAPDH signal, confirming efficient separation from cytosolic components. Conversely, the cytosolic fraction showed strong GAPDH expression and only trace amounts of Na^+/K^+ ATPase, most likely reflecting residual contamination. Importantly, no significant differences in protein marker expression were observed between pre-extrusion and post-extrusion samples. These results confirmed the successful retention of Na^+/K^+ ATPase membrane protein in CCM-NGs from the source cells and indicated that membrane integrity and protein composition were preserved throughout the extrusion process (Fig. S8).

We next examined the retention of functionally relevant membrane proteins, focusing on E-cadherin and CD47. E-cadherin, a key member of the cell adhesion molecule family, plays a pivotal role in cell-cell adhesion by mediating homotypic interactions among tumor cells as well as heterotypic interactions with N-cadherin-expressing CAFs. CD47, often referred to as a "marker of the self", helps tumor cells evade immune clearance and has been associated with prolonged circulation time in nanoparticle formulations [27–29]. In addition to Na^+/K^+ ATPase, immunoblotting confirmed the presence of E-cadherin and CD47 exclusively in the CCM-NGs fraction, supporting the successful transfer and retention of key surface markers from source cells to nanoghosts (Fig. 1d).

3.3. Proteome analysis of CCM-NG

To determine the full protein composition of CCM-NGs and assess the reproducibility across the different production batches, a comprehensive quantitative proteomic analysis was performed. Six independent CCM-NG preparations (F1–F6) were analyzed in technical triplicates by liquid chromatography-mass spectrometry (LC-MS) (Fig. S9). Across all runs, an average of ~5000 proteins were identified per sample. A run identification chart (Fig. 2a) was generated to visualize the number of proteins detected in each replicate run, distinguishing between total identifications and those reproducibly identified in more than 50% of the runs. A total of 4346 proteins were reproducibly identified across F1-F6 dataset, while the number of variably detected proteins ranged from 301 to 400, confirming the high reproducibility of the CCM-NGs production in terms of proteomic content.

Following initial identification, proteins were filtered using stringent

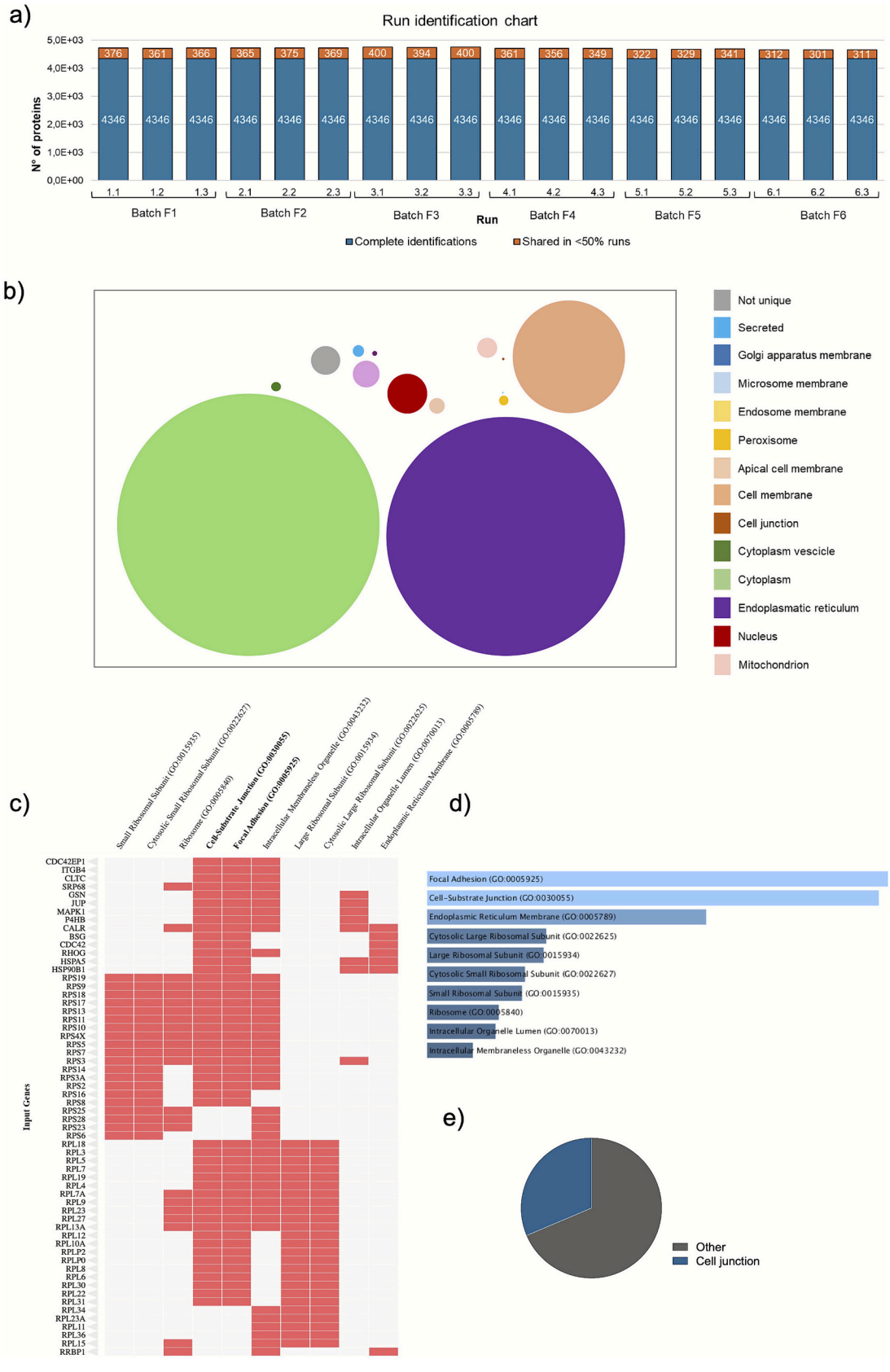

(caption on next page)

Fig. 2. CCM-NG proteome representation. (a) Protein identification consistency across quantitative proteomic analyses of F1-F6 CCM-NGs batches. Each bar represents a single LC-MS/MS run, performed using TIMS-PASEF. Proteomic data refers to $n = 3$ technical replicates for each of the six independent batches. The total number of proteins identified in each run is shown, divided into proteins reproducibly detected in more than 50% of the runs (blue) and those detected in fewer runes (red segment); (b) Cellular localization distribution of the top 148 most abundant proteins (abundance >1000). Protein subcellular localization was determined using UniProt identifiers and enrichment analysis. Each area in the plot represents a distinct cellular compartment, with the size proportional to the cumulative abundance of proteins assigned to that compartment; (c) Clustergram showing the top 10 enriched GO:CC terms and the top 60 most abundant or representative genes (rows), with hierarchical clustering applied to both rows and columns; (d) Gene Ontology (Cellular Component) enrichment analysis of 998 high-confidence proteins identified by proteomic profiling (Enrichr). Bars represent the most significantly enriched GO:CC terms based on *P*-values; (e) Pie chart representing the proportion of total protein abundance (across 998 high-confidence proteins) attributed to the selected GO:CC terms. GO annotations were assigned to each protein, and the abundances of proteins sharing the same GO term were summed. (For interpretation of the references to colour in this figure legend, the reader is referred to the web version of this article.)

selection criteria – including a threshold for coefficient of variation (CV %), sequence count completeness across all batches, and a minimum abundance level (≥100) – to ensure dataset reliability and consistency. This filtering process resulted in the selection of 998 high-confidence proteins. To explore the distribution of the most represented proteins across subcellular compartments, we examined the localization of the top 148 most abundant proteins shared in F1-F6 (abundance >1000) using UniProt annotations and enrichment analysis (Additional UniProt list in Supplementary material 2). As shown in Fig. 2b, these proteins were primarily found in intracellular compartments such as the cytoplasm and endoplasmic reticulum, and displayed notable enrichment at the plasma membrane, reflecting the vesicular and membrane-associated nature of CCM-NGs. The size of each compartmental area in the plot reflects the cumulative abundance of proteins assigned to it, highlighting the dominant subcellular localization within the CCM-NG proteome and supporting their vesicular and membrane-associated identity.

Gene Ontology (Cellular Component) enrichment was performed on the full set of 998 high-confidence and F1-F6 shared proteins. As shown in Fig. 2d, the most significantly enriched GO:CC terms – identified using Enrichr – included focal adhesion and cell-substrate junction, indicating a prominent representation of proteins involved in cell adhesion and extracellular matrix interactions. Consistent enrichment results were obtained using the Compartments Curated (2025) database (Fig. S10). A clustergram (Fig. 2c) of the top 10 enriched GO:CC terms and the 60 most representative proteins (gene names) further illustrated the overlap among related compartments. Several proteins mapped to multiple terms, such as focal adhesion and cell substrate junction, reflecting their multifunctional roles and their association with the dynamic membrane regions from which the vesicles originated. To quantify the contribution of these adhesion-related components, we evaluated the cumulative relative abundance of proteins associated with GO:CC terms related to cell junction (GO:0030054). As shown in Fig. 2e, proteins annotated to focal adhesion, cell-substrate junction and related terms collectively accounted for 31.4% of the total protein abundance, indicating that nearly one-third of the entire CCM-NG proteome is functionally linked to adhesion processes.

Functionally prominent proteins among those identified included cadherins and catenins (e.g., *E*-cadherin, desmoglein-2, junction plakoglobin), integrins (e.g., α2, α3, α5, α6, αV, β1, β2, β4), immunoglobulin superfamily members (e.g., CD44, VCAM-1) as well as galectin-3 and EpCAM, which are well-known mediators of homotypic recognition among cancer cells [30]. VCAM-1, which was highly expressed, is known to mediate heterotypic cell-cell interactions, while CD44 and CD47 contribute to heterotypic adhesion and immune evasion, respectively [31,32]. The consistent detection of Na^+/K^+ ATPase and E-Cadherin at high levels across CCM-NGs batches, in agreement with western blot data, underscores their established roles in maintaining membrane architecture and facilitating cell-cell adhesion [26,27]. Additional enrichment was observed for cytoskeletal scaffolding proteins such as moesin, ezrin, filamin-A, filamin-B, talin-1, and alpha actinin-1, supporting both membrane stability and downstream signaling. Components of tight and adherent junctions – including ZO-2, junctional adhesion molecule A, nectin-2, afadin, and syndecan-1 – were also prominent and could contribute to both homotypic and heterotypic adhesion properties of CCM-NGs. Furthermore, membrane-associated receptors such as basigin (CD147), ephrin type-A and type-B receptors, ADAM10 and ADAM17 metalloproteinases, and protein LYRIC were consistently identified. The predominant presence of these membrane components reflects the preservation of native molecular features essential for tumor-tumor and tumor-stroma interactions, aligning with the bioinspired design strategy of CCM-NGs to retain the biological functionality of their source membranes.

3.4. Identification of CD44 as diagnostic membrane marker in CCM-NGs by single molecule Array (SiMoA)

Among the proteins of interest identified through proteomic analysis, CD44 emerged as one of the most prominent surface markers. CD44 is a cell surface glycoprotein which plays an important role in heterotypic adhesion [31], involved in cell-cell interactions, adhesion, and migration [33]. To validate the proper presentation of this glycoprotein on the surface of CCM-NGs, we analyzed F1-F4 batches from proteomic experiment using digital ELISA.

The Single Molecule Array (SiMoA) platform provided a scalable and user-friendly method for rapid, ultrasensitive quantification of membrane markers. As pan specific capture probe, we selected a well characterized membrane sensing peptide (MSP) derived from bradykinin and known to specifically interact with the phospholipidic bilayer of small extracellular nanoparticles [21,34]. The advantage of this approach resides in integrating SiMoA with the maltose-binding protein (MBP)-based capture agent, which allows extracellular vesicles to be captured independently of their tetraspanin expression levels. To enable specific detection of CD44, we utilized a biotinylated monoclonal antibody to the extracellular domain of CD44 (Fig. 3a).

Nanoparticle tracking analysis (NTA) indicated a particle concentration of approximately 2×10^{11} particles/mL. To achieve a working concentration within the range of 10^7–10^8 particles/mL per well, all samples were diluted 1:5000 prior to incubation. Signals were quantified as fraction of CD44 positive particles over all capture beads. In SiMoA measurements, mean Average Enzyme per Bead (AEB) values greater than 1 correspond to particles carrying more than one molecule of the analyte. As shown in Fig. 3b, all four CCM-NG batches display mean AEB values exceeding 5, indicating exceptionally high levels of CD44 expression on the surface. The consistent signals across all samples highlight the reproducible presence of CD44 in CCM-NGs and support its suitability as a diagnostic membrane marker.

3.5. Validation of CCM-NG membrane protein orientation and functionality

One of the fundamental requirements for preserving nanoghost functionality is the retention of plasma membrane proteins in their native conformation and orientation in CCM-NGs [35]. Given the intrinsic asymmetry of the plasma membrane, incorrect topological arrangement of membrane ligands could impair molecular recognition, binding interactions, and biological activity [36].

To confirm the surface exposure and correct orientation of CD44,

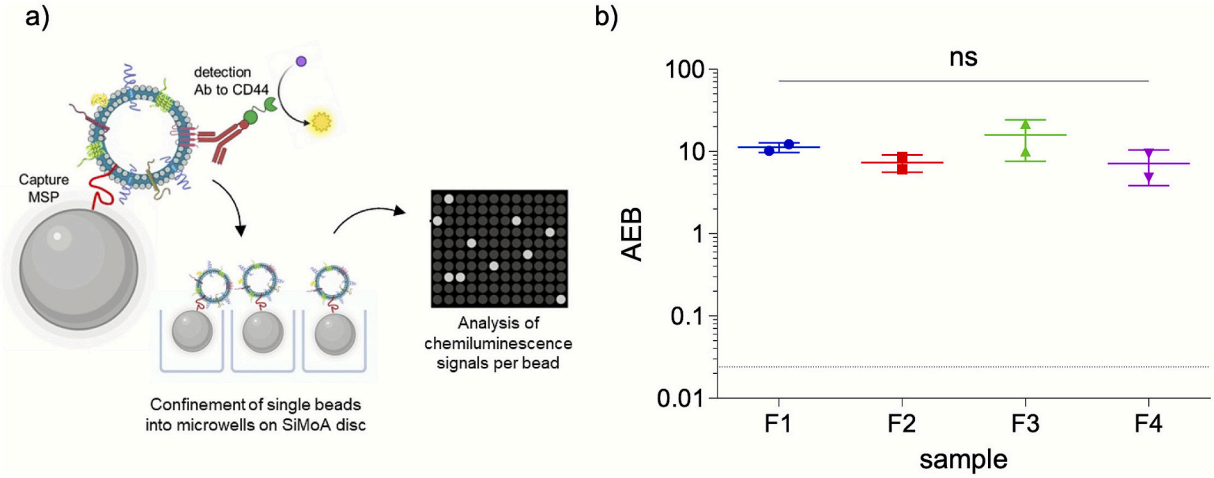

Fig. 3. Identification of CD44 as membrane marker in CCM-NGs by Membrane Sensing Peptides (MSP) based SiMoA assays. (a) Experimental schematic: SiMoA magnetic beads conjugated with MSP were incubated with CCM-NGs and a biotinylated anti-CD44 detection antibody, followed by streptavidin-SBG enzyme to generate chemiluminescent signals on immunocomplex-bearing beads. (b) Average Enzyme per Bead (AEB) signals measured across four independent batches (F1-F4) confirmed consistent high-level expression of CD44 across all batches, indicating robust reproducibility of CCM-NGs production process (dot line = blank). Data represent mean ± SD ($n = 4$ independent batches, each measured in technical duplicate). Statistical analysis was performed using one-way ANOVA followed by multiple comparisons using Tukey's post hoc test: *$p < 0.05$; **$p < 0.01$; ***$p < 0.001$; ****$p < 0.0001$.

CCM-NGs were labeled with lipophilic intercalating fluorescent dyes (DiD and DiO carbocyanine dyes, see Methods section), and their surface was probed for extracellular CD44 epitopes. The binding capacity of labeled CCM-NGs was assessed by incubation with latex beads functionalized with anti-CD44 antibodies recognizing extracellular and conformational epitopes, followed by flow cytometry analysis (Fig. 4a, protocols in SI). A high degree of dye-positive events (96%) was observed for anti-CD44 antibody-coated beads, while control beads functionalized with isotype antibodies showed minimal residual signal (2.7%), confirming specific recognition of surface-exposed CD44 in CCM-NGs. As a negative control, unlabeled CCM-NGs incubated with anti-CD44 antibody-coated beads yielded negligible fluorescence, with no statistically significant difference from the isotype control (Fig. 4b).

Notably, pre-treatment of dye-labeled CCM-NGs with proteinase K (PK) drastically reduced the binding signal to 6%, indicating proteolytic cleavage of accessible extracellular domains, including CD44. This loss of fluorescence confirmed that signal detection was mediated by properly oriented, intact CD44 antigens exposed on the nanoghost surface.

Collectively, these findings demonstrate that CCM-NGs retain key membrane-associated antigens from source cells in their native conformation and correct topological orientation, an essential requirement for recapitulating cell-derived functionalities such as tumor homing and heterotypic targeting.

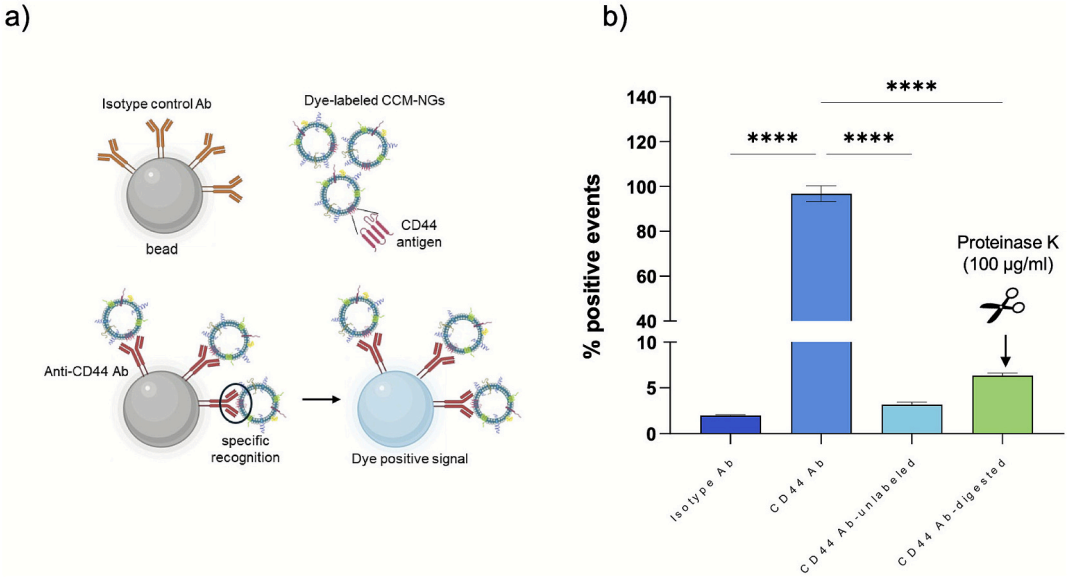

Fig. 4. Validation of membrane protein orientation on CCM-NGs. (a) Schematic illustration of the experimental design; (b) Flow cytometry histograms showing the percentage of dye-positive events. Latex beads functionalized with either anti-CD44 antibodies or isotype control antibodies were incubated with dye-labeled CCM-NGs, unlabeled CCM-NGs, or dye-labeled CCM-NGs pre-treated with Proteinase K (PK). Data are presented as mean ± SD, ($n = 2$ biological replicates; each measured in technical triplicates). Statistical analysis was performed using one-way ANOVA followed by multiple comparisons using Tukey's post hoc test: *p < 0.05; **p < 0.01; ***p < 0.001; ****p < 0.0001.

3.6. CCM-NG-mediated cellular targeting via homotypic and heterotypic recognition

Unlike normal cells, cancer cells exhibit a natural propensity for homotypic adhesion, a key feature contributing to tumor tropism and mass establishment [37]. This process involves intercellular binding among malignant cells and is mediated by cell surface adhesion molecules such as cadherins, selectins, integrins, and Thomsen-Friedenreich antigens. In addition to homotypic aggregation, heterotypic adhesion also plays a pivotal role in tumor progression, facilitating interactions between cancer cells and various TME components, including endothelial and stromal cells, via similar molecular recognition mechanisms [38].

Within desmoplastic tumors, CAFs represent a prominent stromal population and are increasingly recognized as attractive targets for RNA-based therapeutics. Their high abundance, perivascular localization, and active role as drug scavengers within the TME make them a privileged site for targeted delivery [39,40]. CAFs arise from diverse cellular origins, including resident fibroblasts, differentiated precursors, transdifferentiated mature cells, and, in some cases, tumor cells [41]. However, current evidence supports tissue-resident fibroblasts as the predominant source in primary tumors. Direct physical crosstalk between CAFs and cancer cells has been shown to promote tumor invasion through heterotypic junctions involving N-cadherin in CAF membranes and E-cadherin in tumor cells [28]. To investigate heterotypic interactions, we established a CAF model cell culture derived from murine NIH-3 T3 fibroblasts that recapitulated key features of primary CAFs, including elevated expression of alpha smooth muscle actin (α-SMA) [38], a glycolytic metabolic profile, and a distinct elongated morphology.

The cell-specific targeting potential of CCM-NGs, mediated by intrinsic homotypic and heterotypic adhesion mechanisms, was assessed by comparing nanoparticle uptake in 4 T1 TNBC and CAFs. Both cell types were incubated with dye-labeled CCM-NGs for 1, 2, 4, and 6 h, and internalization was quantified by flow cytometry. At each timepoint, nearly 100% of both CAFs and 4 T1 cells were dye-positive, confirming the strong affinity of CCM-NGs for both stromal and tumor cells. Notably, CAFs consistently exhibited significantly higher fluorescence intensity (MFI) compared to 4 T1 cells at all time points, displaying a clear time-dependent increase (Fig. 5). While both cell types demonstrated efficient nanoparticle internalization, the enhanced interaction with CAFs compared to 4 T1 cells suggested the potential involvement of heterotypic adhesion mechanisms, possibly offering a selective advantage for stromal targeting.

Fluorescence microscopy confirmed that, after 1 h incubation, dye-labeled CCM-NGs were efficiently internalized by both CAFs and 4 T1 (Fig. 6). The fluorescent signal appeared as punctate structures predominantly localized in the perinuclear region, consistent with early endosomal compartments (Fig. S15). No fluorescence was observed in cells treated with unlabeled CCM-NGs, confirming the specificity of the signal.

To further evaluate the preferential interaction of CCM-NGs with heterotypic vs. homotypic cell types, a cellular uptake assay was performed using a co-culture model of CAFs and 4 T1 cells. Dye-labeled CCM-NGs were incubated with the co-culture at 37 °C for 5, 10, 20, 30, and 40 min. As shown in Fig. 7a, CAFs internalized higher levels of CCM-NGs compared to 4 T1 cells across all time points analyzed. No fluorescence signal was detected in the control sample treated with unlabeled CCM-NGs (Fig. S16). The experiment was repeated under endocytosis-inhibiting conditions (4 °C), enabling assessment of surface-level interactions. Under these conditions, energy-dependent internalization was suppressed, allowing us to focus on surface binding driven by protein-protein interactions. After removal of unbound CCM, cells were re-incubated at 37 °C for 1 h to allow nanoparticle internalization and detection. Fluorescence was undetectable in samples not re-incubated, confirming the absence of cell internalization at 4 °C (Fig. S17). As shown in Fig. 7b, CCM-NGs exhibited a binding profile similar to that observed under uptake-permissive condition (37 °C), with significantly higher association to CAFs compared to 4 T1 cells. These results further support the notion of selective interaction between CCM-NGs and heterotypic stromal cells, likely mediated by membrane protein recognition.

3.7. Investigation of CCM-NGs membrane protein contribution in hetero- and homotypic cell targeting

Surface proteins in CCM-NGs are known to play a crucial role in mediating interactions with target cells both in homotypic and

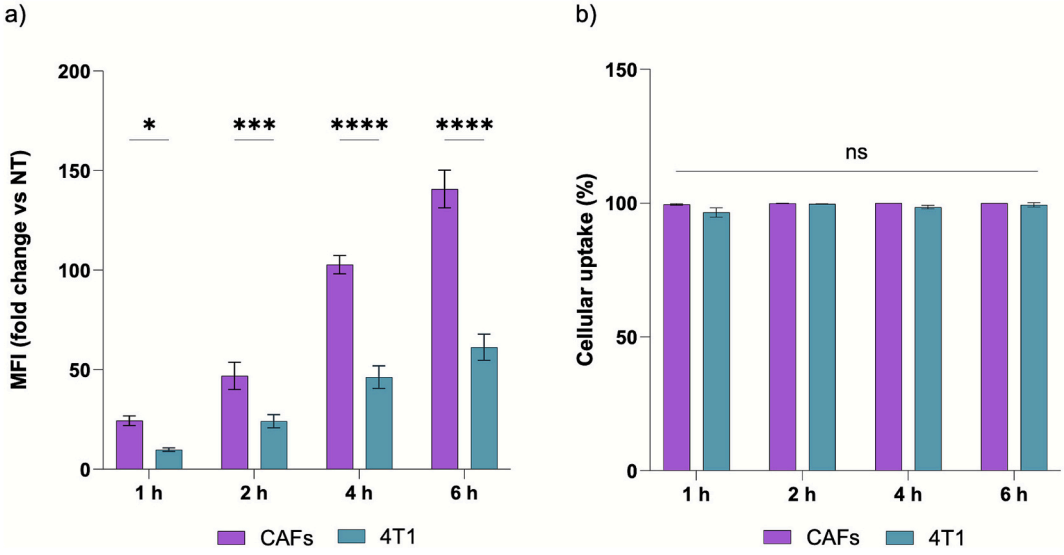

Fig. 5. Flow cytometry analysis of dye-labeled CCM-NGs uptake in CAFs and 4 T1 cells. (a) MFI fold change relative to untreated controls following incubation with dye-labeled CCM-NGs for 1, 2, 4, and 6 h, showing a time-dependent increase and significantly higher MFI in CAFs compared to 4 T1. (b) Percentage of dye-positive cells in CAFs and 4 T1 cells, indicating around 100% uptake across all time points. Data are presented as mean ± SD, ($n = 2$ independent experiments, each performed in technical triplicates). Statistical analysis was performed using two-way ANOVA followed by multiple comparisons using Tukey's post hoc test: *$p < 0.05$; **$p < 0.01$; ***$p < 0.001$; ****$p < 0.0001$.

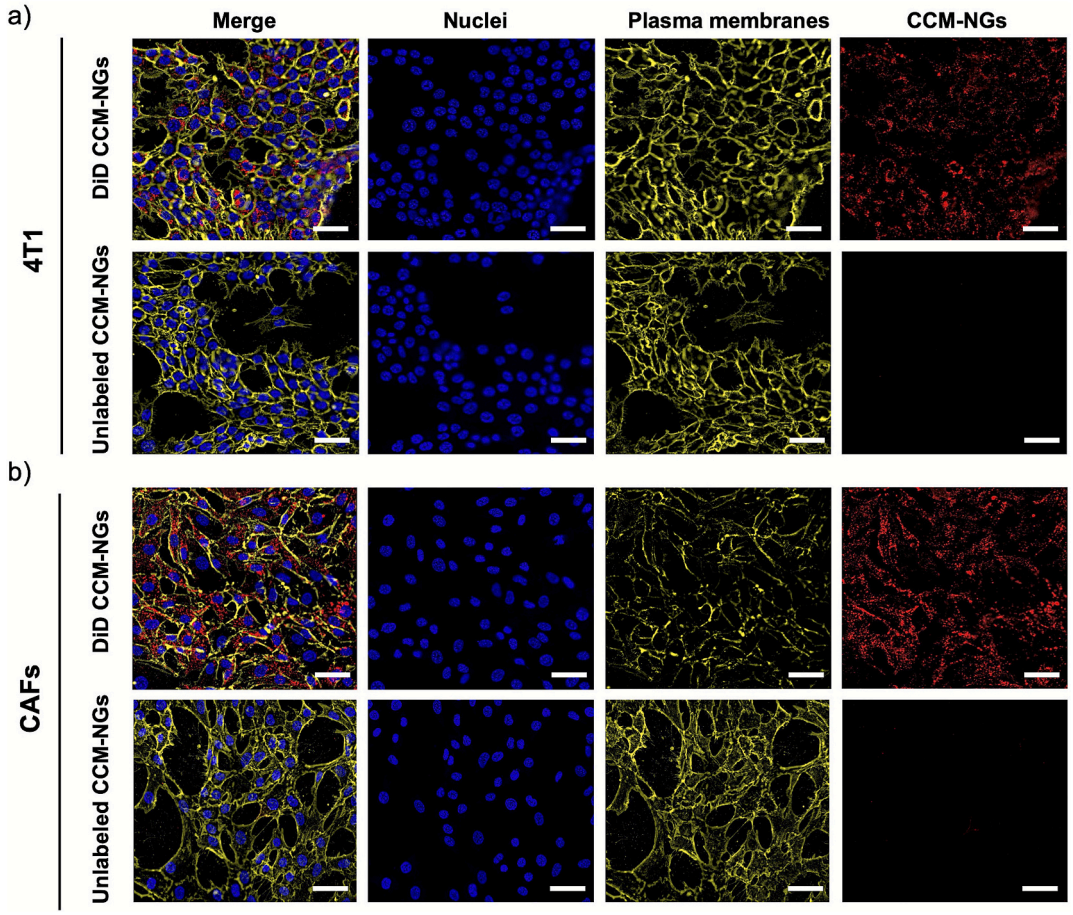

Fig. 6. Cellular uptake of CCM-NGs by CAF and 4 T1 cancer cells. Representative fluorescence microscopy images of (a) 4 T1 cells and (b) CAFs after 1 h incubation with dye-labeled CCM-NGs (top panels) or unlabeled CCM-NGs (bottom panels), acquired using a Thunder Imager. DiD-labeled CCM-NGs are shown in red, nuclei are stained with Hoechst (blue), and plasma membranes are labeled with anti-CD44 antibody (yellow). Scale bars: 50 μm. Images are representative of n = 3 independent experiments. (For interpretation of the references to colour in this figure legend, the reader is referred to the web version of this article.)

heterotypic contexts. By mimicking the native cellular membrane composition, CCM-NGs preserve the functional properties of their source cells, thereby enabling selective engagement with complementary receptors on target cells. These membrane-associated proteins, including transmembrane receptors and adhesion molecules, facilitate specific binding events that are fundamental to cellular recognition,

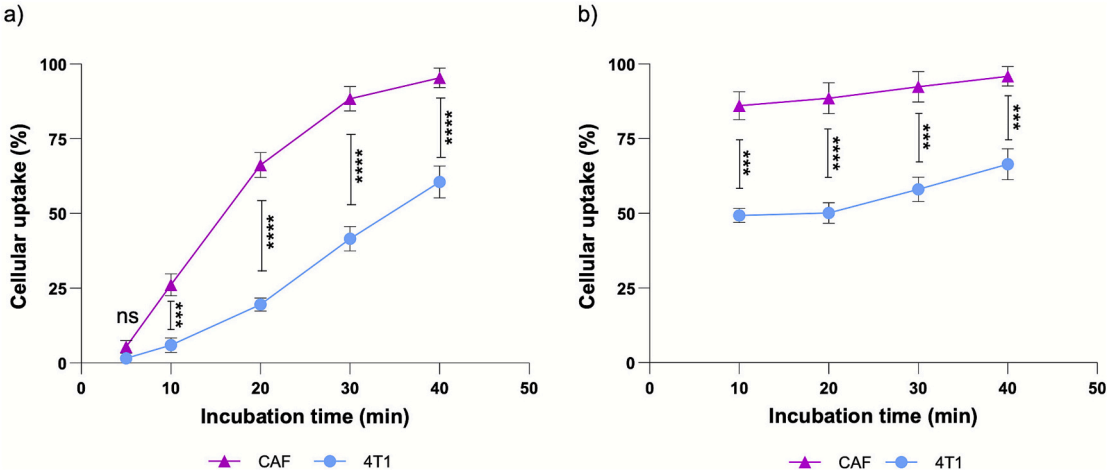

Fig. 7. Preferential interaction of CCM-NGs with heterotypic CAFs in a co-culture model with 4 T1 cells. (a) Time-dependent uptake of dye-labeled CCM-NGs by CAFs and 4 T1 cells incubated in co-culture at 37 °C, as assessed by flow cytometry. CAFs exhibited higher nanoparticle internalization than 4 T1 cells across all time points. (b) Binding assay performed at 4 °C to inhibit active endocytosis, highlighting enhanced surface association of CCM-NGs with CAFs relative to 4 T1 cells, consistent with preferential heterotypic cell recognition. No fluorescence signal was observed in control samples treated with unlabeled CCM-NGs. Data are expressed as the percentage of dye-positive cells and are presented as mean ± SD ($n = 2$ independent experiments, each performed in technical duplicates). Statistical analysis was performed using two-way ANOVA followed by multiple comparisons using Tukey's post hoc test: *$p < 0.05$; **$p < 0.01$; ***$p < 0.001$; ****$p < 0.0001$.

attachment, and subsequent internalization. Here, we aimed to demonstrate the role of membrane-associated proteins retained in CCM-NGs in mediating both homotypic and heterotypic cellular interactions. CCM-NGs were treated with PK, a broad-spectrum serine protease that selectively cleaves accessible extracellular epitopes of the nanovesicle surface proteins. Importantly, PK treatment did not alter the intrinsic fluorescence signal or the physicochemical properties of CCM-NGs, indicating that the structural integrity of the nanovesicles was preserved after proteolytic digestion (Fig. S18). Fluorescence microscopy revealed a pronounced decrease in CCM-NGs uptake by both heterotypic CAFs and homotypic 4 T1 cancer cells following PK digestion (Fig. 8). Similar results were obtained when CCM-NGs were incubated with target cells at 4 °C (binding condition), washed and subsequently re-incubated at 37 °C (uptake condition) (Fig. S19). Under these conditions, CCM-NGs signal was completely lost upon treatment with PK. These findings collectively demonstrate that the interaction between CCM-NGs and target cells was mediated by membrane-associated proteins, both in homotypic and heterotypic targeting. Moreover, the data support the notion that these proteins retain both their native functionality and correct topological orientation following nanoghost fabrication.

The proteolytic digestion analysis illustrated above was conducted in a co-culture of CAFs and 4 T1 cells. The analysis involved incubating dye-labeled CCM-NGs at both 37 °C (uptake condition) and at 4 °C (binding condition). Flow cytometry confirmed a substantial decrease in the uptake of CCM-NGs by both cell populations following proteolytic digestion. Consistently, CAFs exhibited markedly higher internalization of nanoparticles compared to 4 T1 cells under both uptake and binding conditions (Fig. S20). These results further confirm the dual targeting capability of CCM-NGs, highlighting a preferential engagement in heterotypic rather than homotypic interactions.

3.8. Synthesis and characterization of biomimetic RNA-LNPs (BLNPs)

LNPs were integrated with CCM-NGs in a core-shell system (BLNPs). The mRNA encoding the fluorescent reporter protein mCherry was selected as a model oligonucleotide to evaluate the BLNP delivery efficiency. RNA-LNPs were synthesized via microfluidics with precise control over particle size and uniformity (Fig. S21a-b). RNA encapsulation efficiency was quantified by Ribogreen assay (Fig. S21d) and confirmed by gel retardation assay (Fig. S21c). The colloidal stability of mRNA-LNPs was maintained for up to 28 days post-synthesis, as confirmed by DLS measurements after storage at 4 °C (Fig. S22).

As previously outlined, BLNPs were designed to be hybrid core-shell systems, in which mRNA-LNP is the core, while CCM-NG serves as the outer shell. Cell membrane coating has emerged as a robust top-down approach to confer synthetic nanoparticles with the intricate biological functions of natural membranes. Among the established fabrication methods, sonication is widely utilized due to its operational simplicity, scalability, and efficiency in facilitating membrane fusion onto nanoparticle surfaces. The coating of mRNA-LNPs with CCM-NGs was achieved through an optimized protocol involving mixing followed by sonication (Fig. 9a). The size distribution profile of BLNPs, measured by DLS, showed a hydrodynamic size (170 nm) slightly larger compared to mRNA-LNPs (108 nm), consistent with successful association between the LNPs and the membrane-derived vesicles (Fig. 9b). These results are further corroborated by the NTA data reported in Fig. S24. Zeta potential analysis of BLNPs revealed a negative surface charge (−28 mV) similar to that of CCM-NGs, supporting the formation of a core-shell structure. Additionally, the absence of aggregation phenomena was supported by PDI values (Fig. 9b–d). Agarose gel electrophoresis in Fig. 9c showed that sonication of uncoated LNPs led to RNA leakage, likely due to disruption or destabilization of the lipid structure. In contrast, when RNA-LNPs were sonicated together with CCM-NGs, mRNA leakage was negligible, suggesting that the interaction of the two components contributes to the stabilization of the nanoparticle architecture, likely due to a more compact and well-organized assembly. Notably, as shown in Fig. S21e, mRNA integrity was preserved upon sonication, demonstrating that the bath sonication conditions (2 min) selected for BLNP synthesis were carefully optimized to ensure the preservation of nucleic acid stability.

To confirm the formation of hybrid core-shell particles and assess their nanoscale structural features, Small-Angle X-Ray Scattering (SAXS) experiments were performed on CCM-NGs, mRNA-LNPs, and BLNPs. Fig. 9e reports the scattered intensity profile of CCM-NGs and the corresponding model of the form factor, revealing a stratified morphology (core-shell). The shell can be described by a lipid bilayer model, headgroup-tails-headgroup [42] with a total thickness of about 4.7 nm. The fitting parameters are reported in Table S1. The internal electron density is higher than that of the solvent, suggesting that the core contains loosely packed material, as estimate by the intensity decay $I(q) \div q^{-2.2}$, due to the presence of proteins. The intensity profile of mRNA-LNPs is reported in Fig. S23a, showing the expected features of LNPs, with an overall size below 100 nm, a core-shell structure, with an external lipid shell, and an internal core showing an organized internal arrangement (intensity peak at $q = 1.2\ nm^{-1}$), corresponding to a characteristic distance $d = 5.2$ nm [43]. The formation of BLNPs by the sonication procedure was verified on two different samples, measured at different delays from preparation, namely 3 days and a few minutes. The measured intensity spectra (Fig. 9f), were superimposable, indicating strong reproducibility of the preparation and the measurements and a good stability of the hybrid nanoparticles. The intensity profiles of BLNPs were compared in Fig. 9f with the one of a mixed sample obtained by the simple contact of CCM-NGs and mRNA-LNPs. Differences with the sample prepared by simple mixing are small but indicate a different effect of CCM-NGs on the arrangement of LNPs, suggesting an effective interaction between CCM-NGs and mRNA-LNPs upon sonication. Fig. S23b shows that the intensity profile of the mixed sample is superimposable ($q > 0.7\ nm^{-1}$) to the one obtained by the linear sum of the two components (green curve) in the nominal mRNA-to-protein ratio of 12, defined as the ratio between the micrograms of encapsulated mRNA in LNPs and the micrograms of total protein content in CCM-NGs. This ratio corresponds to a number ratio LNPs: CCM-NGs $7.35\ 10^{10}$: $1.12\ 10^{11}$ as evaluated by NTA. The spectra of BLNPs are different and cannot be reconstructed with any different proportion, as shown in Fig. S23d. The peculiar feature is the presence of a more defined internal arrangement in the two BLNPs, although the LNPs batch is the same for all samples.

Parallel measurements were performed on mRNA-LNPs after sonication to test LNP stability. The intensity profile reported in Fig. S23c showed the formation of aggregates and the disappearance of the intensity peak at $q = 1.2\ nm^{-1}$, characteristic of the internal arrangement. The structure of uncoated mRNA-LNPs is unstable when submitted to sonication, in agreement with gel electrophoresis results on RNA leakage (Fig. 9c). Interestingly, the characteristic intensity peak at $q = 1.2\ nm^{-1}$ was visible in BLNP spectra, indicating the stability of the internal arrangement of mRNA-LNPs during sonication in the presence of CCM-NGs. Results suggested the formation of hybrid LNPs coated with CCM-NGs.

Analysis of the BLNP spectra was performed by subtracting the intensity contribution of the fraction of unbounded CCM-NGs, estimated by comparison with the intensity profile of mRNA-LNPs in the high-q region, shaped according to the internal arrangement of the particles (nm lengthscale). The resulting intensity profile, reported in Fig. 9g, showed some distinctive features: the intensity decay $I(q) \div q^{-3}$ in the low q region, a minimum of the intensity profile visible at $q = 0.08\ nm^{-1}$, and the spectrum was similar to the one of mRNA-LNPs in the high-q region. These features indicate the formation of hybrid particles with the internal structure of mRNA-LNPs, a larger size, and an overall morphology compatible with a core-shell arrangement.

Comprehensive physicochemical and structural characterization of BLNPs confirmed the formation of a hybrid nanostructure exhibiting

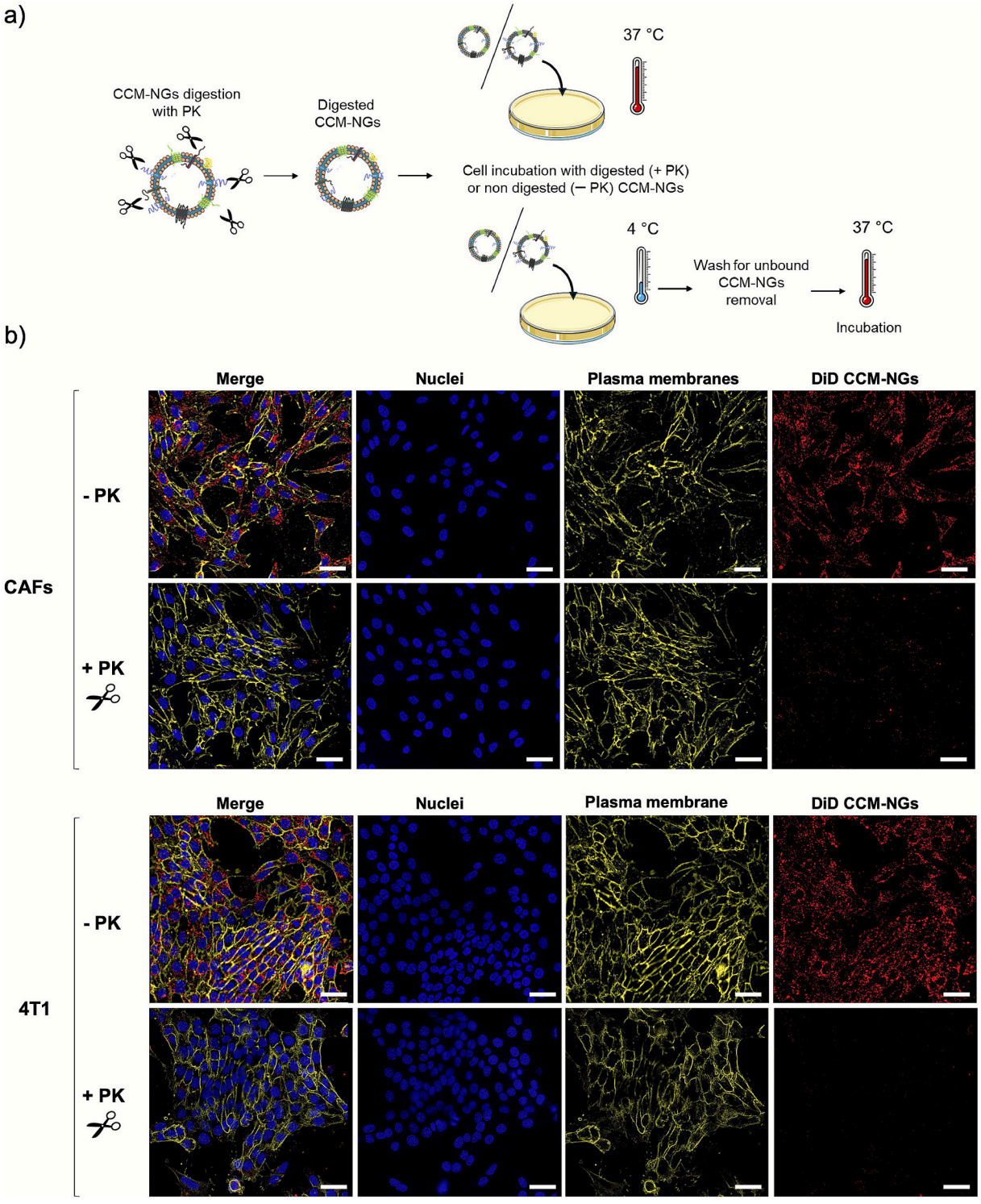

Fig. 8. Role of membrane-associated proteins in CCM-NGs-mediated homotypic and heterotypic targeting. (a) Schematic illustration of the proteolytic digestion protocol. Dye-labeled CCM-NGs were treated with proteinase K (PK) to selectively cleave exposed extracellular domains of membrane-associated proteins and subsequently incubated with target cells under binding (4 °C) or uptake (37 °C) conditions. (b) Representative fluorescence microscopy images of CAFs and 4 T1 cells incubated at 37 °C with dye-labeled CCM-NGs, either untreated (−PK) or PK-digested (+PK). DiD-labeled CCM-NGs are shown in red, cell nuclei were stained with Hoechst (blue), and plasma membranes were immunolabeled with anti-CD44 (yellow). A substantial decrease in CCM-NG internalization was observed upon PK treatment in both cell types, underscoring the pivotal role of membrane proteins in mediating homotypic and heterotypic interactions. Scale bar: 50 μm. Images are representative of n = 3 independent experiments.

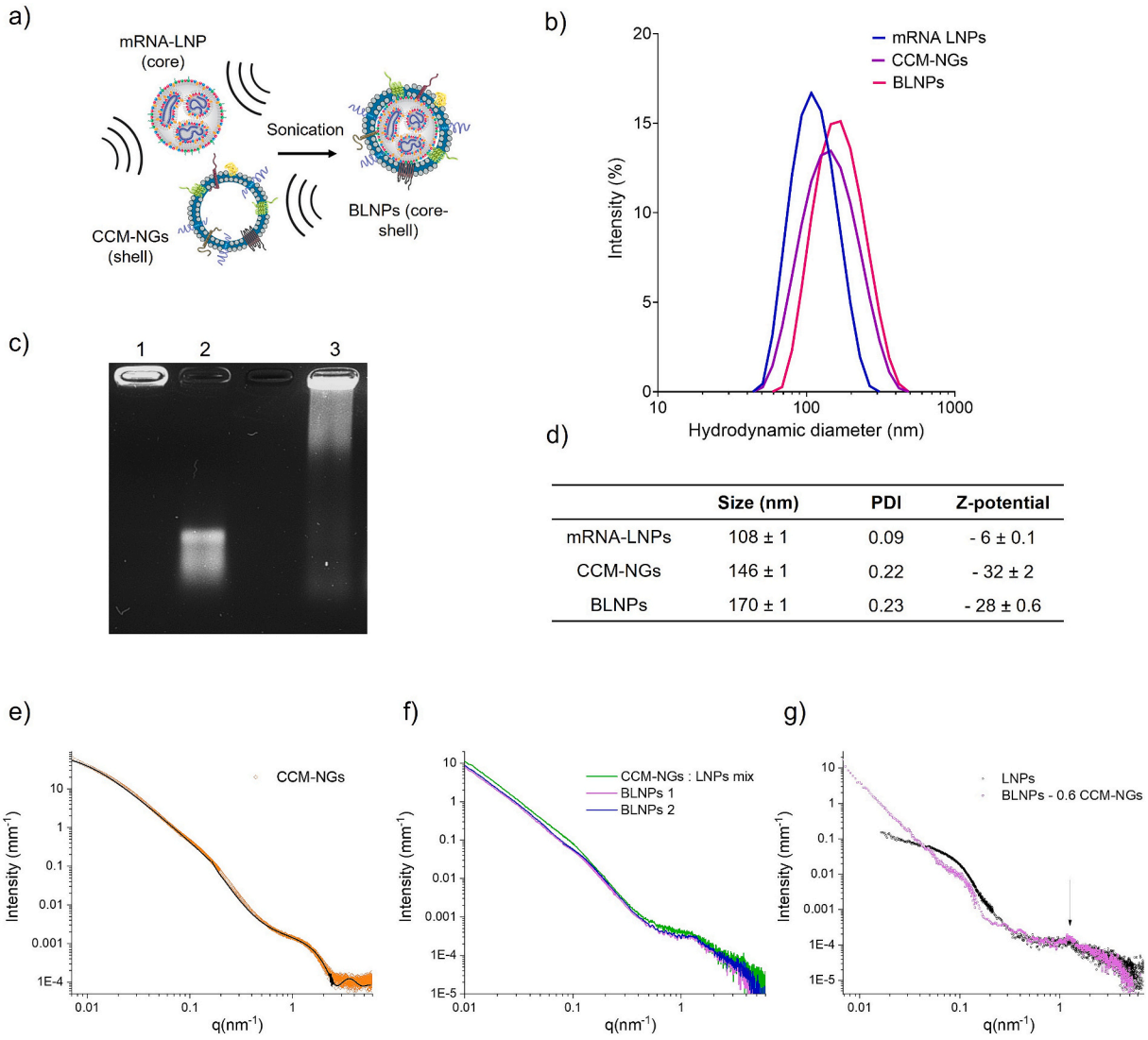

	Size (nm)	PDI	Z-potential
mRNA-LNPs	108 ± 1	0.09	- 6 ± 0.1
CCM-NGs	146 ± 1	0.22	- 32 ± 2
BLNPs	170 ± 1	0.23	- 28 ± 0.6

Fig. 9. Physicochemical characterization of biomimetic lipid nanoparticles (BLNPs). (a) Schematic representation of BLNPs production via sonication of mRNA LNPs with CCM-NGs. (b) Hydrodynamic size distribution profiles of mRNA-LNPs, CCM-NGs and BLNPs, measured by DLS. Data are presented as mean ± SD (n = 3 independent measurements). (c) Agarose gel electrophoresis (1.2%) assessing RNA retention following sonication. Lane 1: intact LNPs; lane 2: sonicated LNPs, showing RNA leakage due to lipid destabilization; lane 3: BLNPs, showing retained RNA, indicative of LNPs integrity and stability conferred by CCM-NGs coating. Gel image is representative of n = 2 independent experiments. (d) Size, PDI and *Z*-potential of formulations as measured by DLS. Data are presented as mean ± SD (n = 3 independent measurements). SAXS intensity profiles of (e) CCM-NGs (orange diamonds) and the fit (black line) obtained with a core shell model ($q > 0.2$ nm^{-1}) and with a mass-fractal model ($q < 0.2$ nm^{-1}); (f) CCM-NGs: LNPs sample obtained by simple mixing (green), BLNPs 1 (3 days from the preparation, light magenta), BNLs 2 (just prepared, blue); (g) LNPs (black line), BNLs after subtraction of the intensity contribution of the non-interacting CCM-NGs fraction (light magenta squares). (For interpretation of the references to colour in this figure legend, the reader is referred to the web version of this article.)

properties that are distinct from those of both bare LNPs and CCM-NG alone. The BLNP structure can be described as mRNA-LNP core surrounded by a CCM-NG envelope. Synthesized BLNPs, as well as their individual LNP and CCM-NG components, were successfully assessed by cell viability assay to demonstrate their safety in CAF and 4 T1 cell cultures (Fig. S25).

3.9. BLNPs uptake in CAFs

The role of biomimetic coating in enhancing cellular uptake in CAFs was investigated by fluorescence microscopy. LNPs and CCM-NGs were differently labeled (Cy5 and DiO, respectively). The structural integration of the hybrid nanovector components was evaluated by analyzing the spatial co-localization of fluorescent signals associated with LNP core and CCM-NGs. To this end, CAFs were incubated with BLNPs, CCM-NGs, or uncoated LNPs and imaged by fluorescence microscopy. This investigation was complemented by PK digestion assay, as described above. As shown in Fig. 10b, Cy5 fluorescence (red) was absent in cells treated with uncoated LNP, indicating negligible uptake. In contrast, DiO fluorescence (green) was clearly detected in CAFs treated with CCM-NGs, confirming efficient internalization of the biomimetic vesicles when membrane proteins were preserved (Fig. 10a). Notably, cells treated with BLNPs displayed both red and green fluorescence signals (Fig. 10c) with a high degree of intracellular co-localization. Quantitative image analysis using Manders' coefficient revealed high colocalization values (tM1 = 0.82 ± 0.03; tM2 = 0.91 ± 0.04, *n* = 3 regions), supporting the hypothesis of a structurally integrated core–shell nanoparticle architecture (Fig. 11). However, following PK digestion, neither red nor green fluorescence signals were observed in the BLNP sample, confirming the pivotal role of surface-exposed and protease-sensitive membrane proteins in mediating cellular interaction. Surprisingly, cells incubated with the physical mixture of LNPs and CCM-NGs were

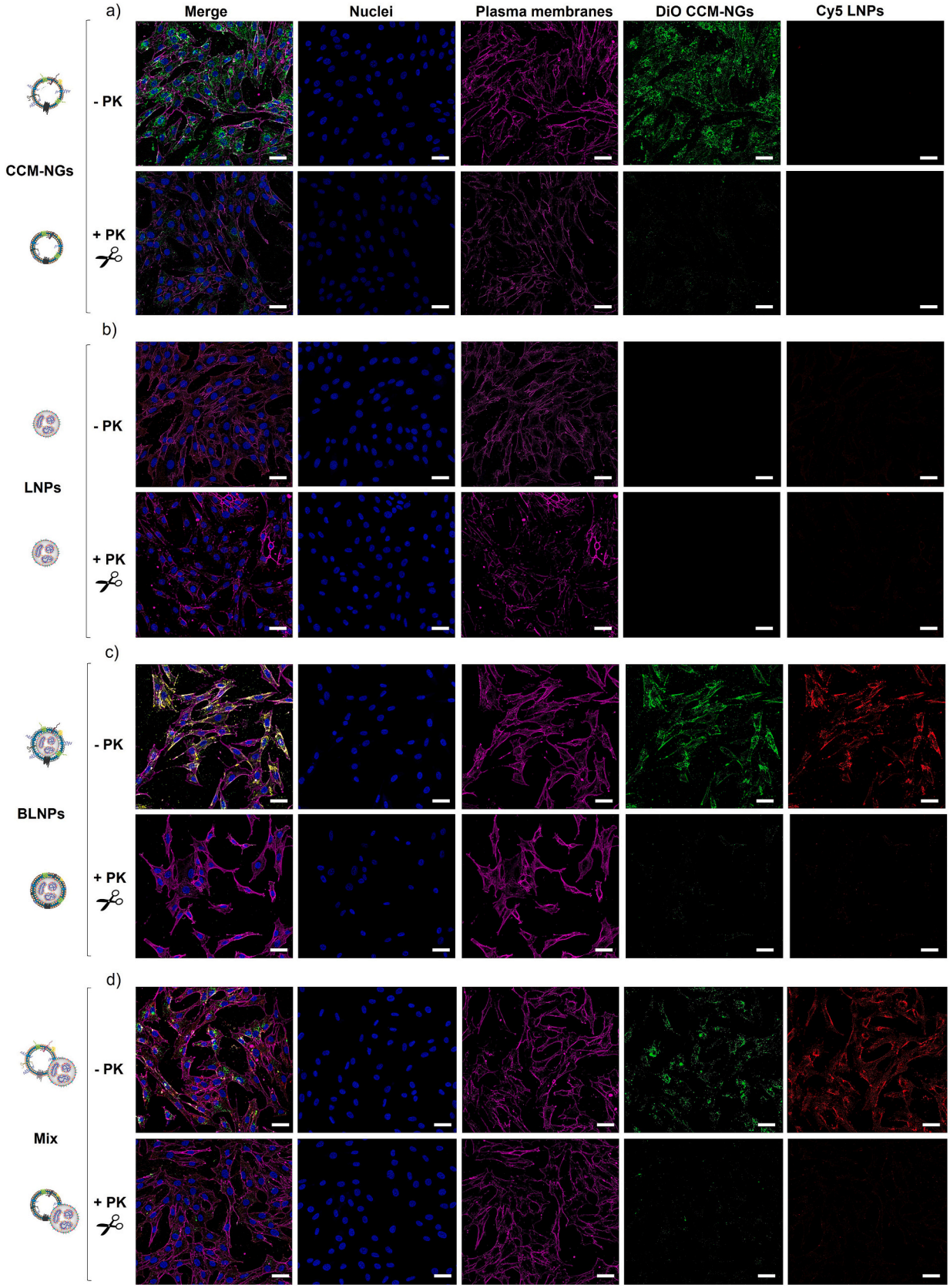

Fig. 10. BLNPs uptake in CAFs. Representative fluorescence microscopy images of CAFs incubated with DiO-labeled CCM-NGs (a), Cy5-LNPs (b), BLNPs (c), and the physical mixture of LNPs and CCM-NGs (d), either untreated (−PK) or digested with proteinase K (+PK). DiO-labeled CCM-NGs are depicted in green, Cy5-LNPs in red, nuclei were stained with Hoechst (blue) and the plasma membrane was stained with anti-CD44 Ab (magenta). Co-localization of red and green signals in the BLNP (−PK) sample indicates integrated core-shell nanoparticle uptake. Scale bar: 50 μm. Images are representative of n = 3 independent experiments. (For interpretation of the references to colour in this figure legend, the reader is referred to the web version of this article.)

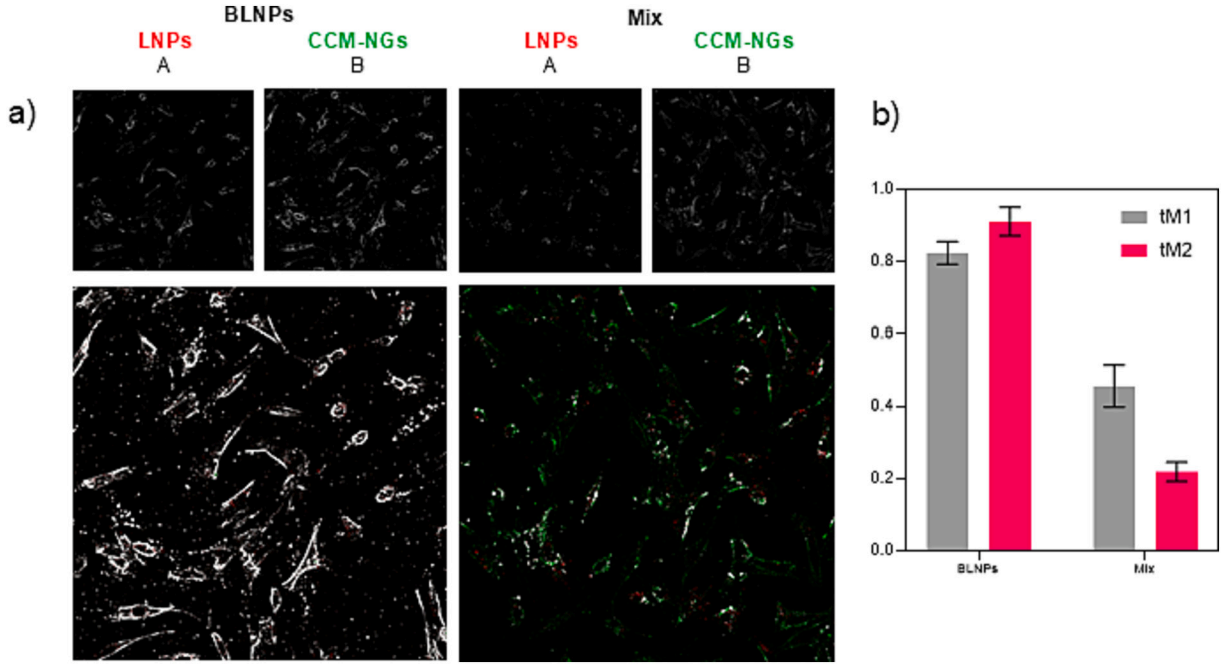

Fig. 11. Manders' colocalization analysis of CCM-NGs and LNPs signals in BLNPs and mix samples. (a) Representative images of fluorescent signals from CCM-NGs (channel B) and LNPs (channel A), converted to 8-bit grayscale and processed with background subtraction (rolling ball = 15 pixels). Below, the colocalization map generated with ImageJ: white indicates colocalized signals, while green and red correspond to CCM-NG-only and LNP-only signals, respectively; (b) Histogram representing the average colocalization values: For Mix sample tM1 = 0.46 ± 0.06 and tM2 = 0.22 ± 0.026 calculated across 4 regions; For BLNP sample tM1 = 0.82 ± 0.03 and tM2 = 0.91 ± 0.04 calculated across 3 regions. tM1 (Thresholded Manders' Coefficient (1) quantifies the fraction of Channel A (LNPs) fluorescence overlapping with Channel B (CCM-NGs), while tM2 (Thresholded Manders' Coefficient (2) quantifies the reciprocal fration of Channel B overlapping with Channel A. Values of both coefficients close to 1 indicate a high degree of colocalization, consistent with BLNPs composed of an LNP core enveloped by a CCM-NG shell. (For interpretation of the references to colour in this figure legend, the reader is referred to the web version of this article.)

able to internalize both nanoparticles (Fig. 10d). Consistently, LNPs were no longer internalized upon treatment of the mixture with PK. This result suggested that LNPs uptake was mediated by some degree of interaction with CCM-NGs. Nonetheless, in this case, no co-localization between LNPs and CCM-NGs was observed. In line with this, Manders' coefficients revealed low co-localization for the mixture condition (tM1 = 0.46 ± 0.06; tM2 = 0.22 ± 0.02, n = 4 regions), consistent with independent internalization events rather than hybrid structure formation (Fig. 11 and Fig. S26). Collectively, these findings indicated that CCM-NG coating was necessary to promote LNP internalization in CAFs, which was otherwise negligible using uncoated LNPs. The marked difference in uptake between the digested (+PK) and undigested (−PK) BLNPs provided indirect yet compelling evidence of a core-shell architecture, in which the outer shell composed of CCM-NGs promotes heterotypic targeting through surface-exposed membrane proteins.

3.10. BLNPs enhance transfection efficiency in CAFs and 4 T1 cancer cells

The transfection efficiency of BLNPs was evaluated by quantifying the expression of the reporter protein mCherry via flow cytometry. CAFs and 4 T1 cells were incubated with either mRNA-BLNPs or uncoated mRNA-LNPs, and mCherry fluorescence was measured at 24, 48, and 72 h post-transfection.

As shown in Fig. 12a–c, CAFs treated with uncoated LNPs displayed negligible mCherry fluorescence at all time points, consistent with the uptake data. In contrast, cells transfected with BLNPs exhibited a substantial increase in mCherry expression over time, with a fluorescence peak detected at 72 h post-treatment. These findings suggested selective recognition and improved intracellular trafficking of BLNPs, which were also presumed to mediate endosomal escape, thereby enabling efficient and successful mRNA translation. In 4 T1 cells, a low but detectable level of mCherry expression was observed following treatment with uncoated LNPs. Nevertheless, transfection efficiency was markedly improved with BLNPs at 72 h post-transfection (Fig. 12b–d), indicating that biomimetic coating enhanced delivery performance across both stromal and cancer cell populations.

4. Conclusion

In this work, we demonstrate a significant conceptual and technological advance in the engineering of biomimetic lipid nanoparticles (BLNPs) by integrating RNA-loaded lipid nanoparticles with cancer cell membrane-derived nanoghosts (CCM-NGs). The combination of microfluidic lipid nanoparticle (LNP) fabrication with membrane cloaking via ultrasound-assisted fusion yielded structurally defined BLNPs that preserved both the multilamellar internal architecture of LNPs and the native orientation of key membrane proteins from tumor cells. Detailed physicochemical, biochemical, and proteomic analyses confirmed the structural stability and biological functionality of CCM-NGs, supporting their ability to mediate specific cell recognition. This biomimetic coating endowed the nanocarriers with enhanced biocompatibility, immune evasion, and, importantly, enabled both homotypic and heterotypic targeting within the tumor microenvironment (TME).

A key innovation of this study lies in demonstrating that membrane proteins naturally present on cancer cell membranes can be harnessed not only for homotypic tumor-tumor recognition – widely explored in previous cancer cell membrane cloaking studies [14,16,17] – but also to achieve heterotypic tumor-stroma targeting, particularly toward cancer-associated fibroblasts (CAFs). Through comprehensive proteomic profiling, structural validation (including Small-Angle X-ray Scattering, SAXS), and functional assays, we provide compelling evidence that BLNPs can selectively recognize and internalize into both 4 T1 breast cancer cells and CAFs. This represents a substantial improvement over

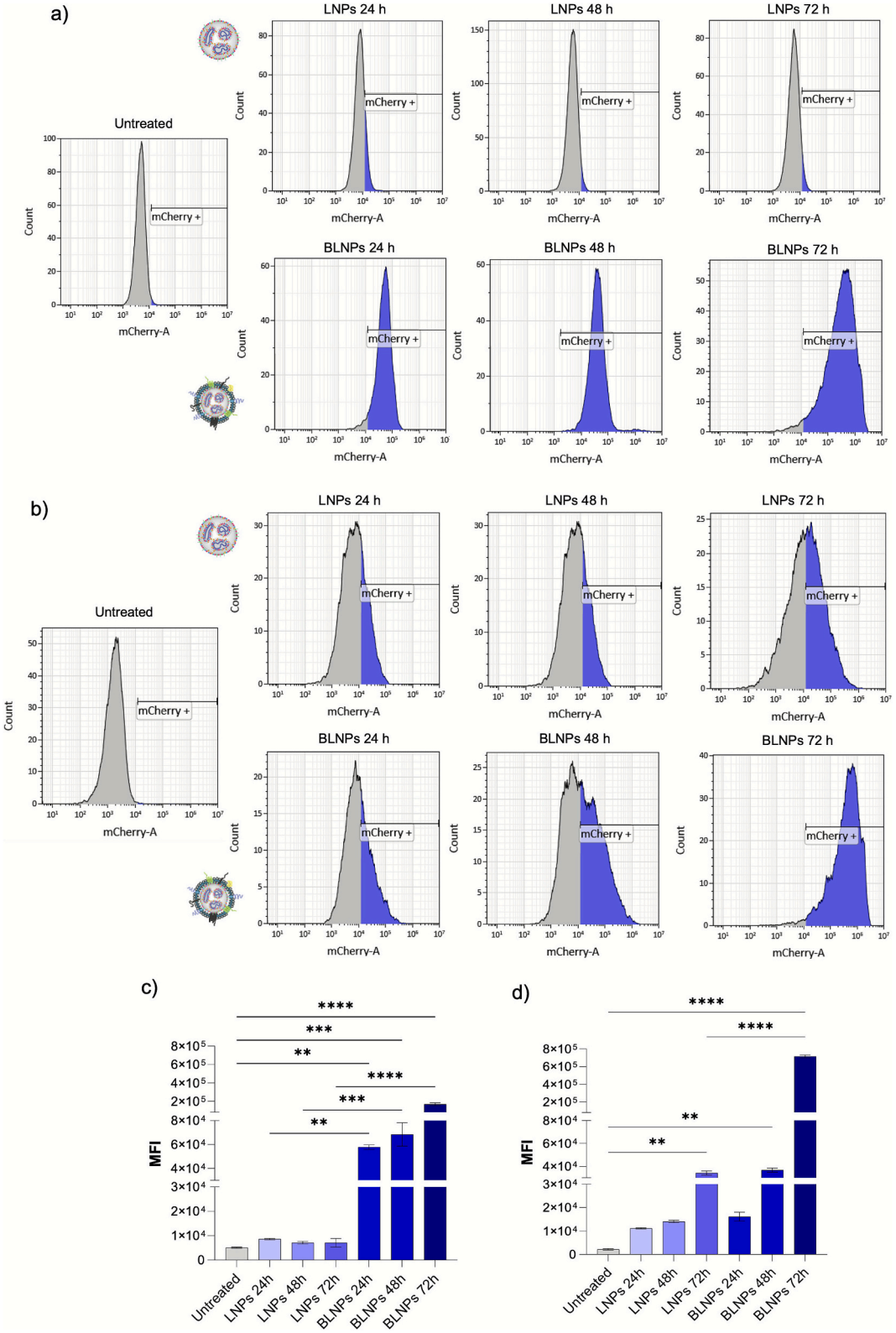

Fig. 12. BLNPs enhance transfection efficiency in CAFs and 4 T1. Flow cytometry analysis of mCherry expression in CAFs (a) and 4 T1 cancer cells (b) transfected with uncoated LNPs (top row) or BLNPs (bottom row). mCherry fluorescence was measured at 24, 48, and 72 h post-transfection. Blue histograms indicate mCherry-positive cells (threshold set based on untreated control). Quantification of mCherry expression levels in CAFs (c) and 4 T1 cells (d) is shown as arithmetic mean fluorescence intensity (MFI). Data represent mean ± SD ($n = 2$ independent experiments, each performed in technical duplicates). Statistical analysis was performed using one-way ANOVA. Significance is reported only for comparisons within the same timepoint: untreated vs. LNPs or BLNPs, and LNPs vs. BLNPs. *p < 0.05, **p < 0.01, ***p < 0.001, ****p < 0.0001. (For interpretation of the references to colour in this figure legend, the reader is referred to the web version of this article.)

conventional LNPs, which showed negligible interaction with stromal cells and only limited uptake in tumor cells.

Compared to previous approaches using membrane-coated nanoparticles – primarily focused on circulation time and homotypic tumor accumulation – our findings establish a distinct conceptual advance: biomimetic vesicles intrinsically leverage heterotypic adhesion mechanisms that govern tumor-stroma crosstalk. This property expands the applicability of membrane camouflaging strategies and addresses major limitations of LNP-based RNA therapeutics, including poor targeting and low bioavailability in desmoplastic tumors, where stromal barriers play a dominant role.

The enhanced uptake and transfection efficiency observed for BLNPs in both CAFs and 4 T1 cells highlight their potential for the selective delivery of genetic payloads to multiple, functionally relevant TME components. These advances open promising opportunities to leverage natural adhesion pathways to modulate the TME, improve RNA distribution, and enhance gene therapy efficacy in challenging cancers such as triple-negative breast cancer.

Future efforts will focus on in vivo evaluation of BLNP biodistribution and pharmacokinetics, optimization of membrane-lipid fusion parameters, and incorporation of therapeutic RNA cargos aimed at stromal reprogramming or combined tumor-stroma targeting. Collectively, our results establish a robust framework for the rational design of biomimetic LNP systems and demonstrate their potential as next-generation RNA delivery platforms with improved selectivity, stability, and translational potential.

CRediT authorship contribution statement

Stefania Garbujo: Writing – original draft, Visualization, Validation, Methodology, Investigation, Data curation. **Chiara Baioni:** Validation, Investigation. **Andrea Banfi:** Validation, Formal analysis. **Leonardo Bolis:** Investigation. **Giulia Bonvini:** Investigation. **Elena Del Favero:** Investigation, Formal analysis, Data curation, Conceptualization. **Paola Gagni:** Investigation. **Alessandro Gori:** Methodology, Formal analysis. **Linda Barbieri:** Investigation. **Marco Davide Giustra:** Validation. **Giulia Tomaino:** Formal analysis. **Lucia Morelli:** Formal analysis. **Clizia Chinello:** Investigation. **Fulvio Magni:** Writing – review & editing. **Lucia Salvioni:** Methodology, Investigation, Data curation, Conceptualization. **Miriam Colombo:** Writing – review & editing, Supervision, Resources, Project administration, Funding acquisition. **Davide Prosperi:** Writing – review & editing, Writing – original draft, Supervision, Project administration, Funding acquisition, Conceptualization.

Declaration of competing interest

The authors declare that they have no known competing financial interests or personal relationships that could have appeared to influence the work reported in this paper.

Acknowledgements

This work was financially supported by AIRC under IG 2021 (project ID 21565), the European Union – NextGenerationEU through the Italian Ministry of University and Research under PNRR – M4C2-I1.4 Project CN3 “National Center for Gene Therapy and Drugs based on RNA Technology”, CUP H43C22000500001, and by the Italian Ministry of University and Research under the PRIN 2022 program (Project No. 2022BLLAEX). The authors are grateful to Dan Peer (University of Tel-Aviv) for help in LNPs synthesis, manipulation and characterization and Tiziano Catelani (University of Milano-Bicocca) for TEM imaging. The authors thank ESRF for beamtime and support and ID02 staff for technical assistance.

Appendix A. Supplementary data

Supplementary data to this article can be found online at https://doi.org/10.1016/j.jcis.2026.139972.

Data availability

Data will be made available on request.

References

[1] V. Singh, N. Khan, G.R. Jayandharan, Vector engineering, strategies and targets in cancer gene therapy, Cancer Gene Ther. 29 (5) (2022) 402–417, https://doi.org/10.1038/s41417-021-00331-7.
[2] Y. Li, S. Zhou, Q. Wu, C. Gong, CRISPR/Cas gene editing and delivery systems for cancer therapy, WIREs Nanomed. Nanobiotech. 16 (1) (2024) e1938, https://doi.org/10.1002/wnan.1938.
[3] K. Paunovska, D. Loughrey, J.E. Dahlman, Drug delivery systems for RNA therapeutics, Nat. Rev. Genet. 23 (5) (2022) 265–280, https://doi.org/10.1038/s41576-021-00439-4.
[4] H. Ritchie, Coronavirus (COVID-19) Vaccinations – Our World in Data, can be found under, https://ourworldindata.org/covid-vaccinations, 2020. accessed: October 24, 2025.
[5] X. Hou, R. Langer, Y. Dong, Lipid nanoparticles for mRNA delivery, Nat. Rev. Mater. 6 (12) (2021) 1078–1094, https://doi.org/10.1038/s41578-021-00358-0.
[6] K.A. Hajj, K.A. Whitehead, Tools for translation: non-viral materials for therapeutic mRNA delivery, Nat. Rev. Mater. 2 (10) (2017) 1–17, https://doi.org/10.1038/natrevmats.2017.56.
[7] B. Li, X. Zhang, Y. Dong, Nanoscale platforms for messenger RNA delivery, WIREs Nanomed. Nanobiotech. 11 (2) (2019) e1530, https://doi.org/10.1002/wnan.1530.
[8] Let's talk about lipid nanoparticles, Nat. Rev. Mater. 6 (2021) 99, https://doi.org/10.1038/s41578-021-00281-4.
[9] A. Wittrup, A. Ai, X. Liu, P. Hamar, R. Trifonova, K. Charisse, M. Manoharan, T. Kirchhausen, J. Lieberman, Visualizing lipid-formulated siRNA release from endosomes and target gene knockdown, Nat. Biotechnol. 33 (8) (2015) 870–976, https://doi.org/10.1038/nbt.3298.
[10] R. Kularatne, R.M. Crist, S.T. Stern, The future of tissue-targeted lipid nanoparticle-mediated nucleic acid delivery, Pharmaceuticals 15 (7) (2022) 897, https://doi.org/10.3390/ph15070897.
[11] L.T. Johnson, D. Zhang, K. Zhou, S.M. Lee, S. Liu, S.A. Dilliard, L. Farbiak, S. Chatterjee, Y.-H. Lin, D.J. Siegwart, Nanoparticle (LNP) chemistry can endow unique in vivo RNA delivery fates within the liver that alter therapeutic outcomes in a cancer model, Mol. Pharm. 19 (11) (2022) 3973–3986, https://doi.org/10.1073/pnas.2109256118.
[12] J. Di, Z. Du, K. Wu, S. Jin, X. Wang, T. Li, Y. Xu, Biodistribution and non-linear gene expression of mRNA LNPs affected by delivery route and particle size, Pharm. Res. 39 (1) (2022) 105–114, https://doi.org/10.1007/s11095-022-03166-5.
[13] S.A. Dilliard, Q. Cheng, D.J. Siegwart, On the mechanism of tissue-specific mRNA delivery by selective organ targeting nanoparticles, Proc. Natl. Acad. Sci. USA 118 (52) (2021) e2109256118, https://doi.org/10.1073/pnas.2109256118.
[14] Q. Guo, S. Wang, R. Xu, Y. Tang, X. Xia, Cancer cell membrane-coated nanoparticles: a promising anti-tumor bionic platform, RSC Adv. 14 (15) (2024) 10608–10637, https://doi.org/10.1039/d4ra01026d.
[15] J. Gallo, A. Villasante, Recent advances in biomimetic nanocarrier-based photothermal therapy for cancer treatment, Int. J. Mol. Sci. 24 (20) (2023) 15484, https://doi.org/10.3390/ijms242015484.
[16] L. Liu, D. Pan, S. Chen, M.-V. Martikainen, A. Kårlund, J. Ke, H. Pulkkinen, H. Ruhanen, M. Roponen, R. Käkelä, W. Xu, J. Wang, V.-P. Lehto, Systematic design of cell membrane coating to improve tumor targeting of nanoparticles, Nat. Commun. 13 (1) (2022) 6181, https://doi.org/10.1038/s41467-022-33889-3.
[17] Z. Liu, F. Wang, X. Liu, Y. Sang, L. Zhang, J. Ren, X. Qu, Cell membrane-camouflaged liposomes for tumor cell-selective glycans engineering and imaging in vivo, Proc. Natl. Acad. Sci. USA 118 (30) (2021) e2022769118, https://doi.org/10.1073/pnas.2022769118.
[18] F. Pelon, B. Bourachot, Y. Kieffer, I. Magagna, F. Mermet-Meillon, I. Bonnet, A. Costa, A.-M. Givel, Y. Attieh, J. Barbazan, C. Bonneau, L. Fuhrmann, S. Descroix, D. Vignjevic, P. Silberzan, M.C. Parrini, A. Vincent-Salomon, F. Mechta-Grigoriou, Cancer-associated fibroblast heterogeneity in axillary lymph nodes drives metastases in breast cancer through complementary mechanisms, Nat. Commun. 11 (1) (2020) 404, https://doi.org/10.1038/s41467-019-14134-w.
[19] Y. Chen, K.M. McAndrews, R. Kalluri, Clinical and therapeutic relevance of cancer-associated fibroblasts, Nat. Rev. Clin. Oncol. 18 (12) (2021) 792–804, https://doi.org/10.1038/s41571-021-00546-5.
[20] Y. Chen, J. Kim, S. Yang, H. Wang, C.-J. Wu, H. Sugimoto, V.S. LeBleu, R. Kalluri, Type I collagen deletion in αSMA^{+} myofibroblasts augments immune suppression and accelerates progression of pancreatic cancer, Cancer Cell 39 (4) (2021) 548–556.e6, https://doi.org/10.1016/j.ccell.2021.02.007.
[21] A. Gori, A. Romanato, G. Bergamaschi, A. Strada, P. Gagni, R. Frigerio, D. Brambilla, R. Vago, S. Galbiati, S. Picciolini, M. Bedoni, G.G. Daaboul, M. Chiari, M. Cretich, Membrane-binding peptides for extracellular vesicles on-chip analysis, J. Extracell. Vesicles 9 (2020) 1751428, https://doi.org/10.1080/20013078.2020.1751428.

[22] J. Jin, B. Krishnamachary, J.D. Barnett, S. Chatterjee, D. Chang, Y. Mironchik, F. Wildes, E.M. Jaffe, S. Nimmagadda, Z. Bhujwalla, Human cancer cell membrane-coated biomimetic nanoparticles reduce fibroblast-mediated invasion and metastasis and induce T-cells, ACS Appl. Mater. Interfaces 11 (8) (2019) 7850–7861, https://doi.org/10.1021/acsami.8b22309.
[23] P. Previtali, L. Pagani, G. Risca, G. Capitoli, E. Bossi, G. Oliveira, I. Piga, A. Radice, B. Trezzi, R.A. Sinico, F. Magni, C. Chinello, Towards the definition of the molecular hallmarks of idiopathic membranous nephropathy in serum proteome: a DIA-PASEF approach, Int. J. Mol. Sci. 24 (14) (2023) 11756, https://doi.org/10.3390/ijms241411756.
[24] C. Ricci, E. Del Favero, Biomimetic lipid nanoparticles for RNA delivery (version 1) [dataset], European Synchrotron Radiation Facility, 2025, https://doi.org/10.15151/ESRF-DC-2222729891.
[25] L. Rao, L.-L. Bu, B. Cai, J.-H. Xu, A. Li, W.-F. Zhang, Z.-J. Sun, S.-S. Guo, W. Liu, T.-H. Wang, X.-Z. Zhao, Cancer cell membrane-coated upconversion nanoprobes for highly specific tumor imaging, Adv. Mater. 28 (18) (2016) 3460–3466, https://doi.org/10.1002/adma.201506086.
[26] S.A. Rajasekaran, L.G. Palmer, S.Y. Moon, A. Peralta Soler, G.L. Apodaca, J. F. Harper, Y. Zheng, A.K. Rajasekaran, Na, K-ATPase activity is required for formation of tight junctions, desmosomes, and induction of polarity in epithelial cells, Mol. Biol. Cell 12 (12) (2001) 3717–3732, https://doi.org/10.1091/mbc.12.12.3717.
[27] E. Bullock, V.G. Brunton, E-cadherin-mediated cell-cell adhesion and invasive lobular breast cancer, Adv. Exp. Med. Biol. 1464 (2025) 259–275, https://doi.org/10.1007/978-3-031-70875-6_14.
[28] A. Labernadie, T. Kato, A. Brugués, et al., A mechanically active heterotypic E-cadherin/N-cadherin adhesion enables fibroblasts to drive cancer cell invasion, Nat. Cell Biol. 19 (3) (2017) 224–237, https://doi.org/10.1038/ncb3478.
[29] F. Wu, H. Pang, F. Li, M. Hua, C. Song, J. Tang, Progress in cancer research on the regulator of phagocytosis CD47, which determines the fate of tumor cells, Oncol. Lett. 27 (6) (2024) 256, https://doi.org/10.3892/ol.2024.14389.
[30] B. Yu, X. Xue, Z. Yin, L. Cao, M. Li, J. Huang, Engineered cell membrane-derived nanocarriers: the enhanced delivery system for therapeutic applications, Front. Cell Dev. Biol. 10 (2022) 844050, https://doi.org/10.3389/fcell.2022.844050.
[31] Q. Lin, Y. Peng, Y. Wen, X. Li, D. Du, W. Dai, W. Tian, Y. Meng, Recent progress in cancer cell membrane-based nanoparticles for biomedical applications, Beilstein J. Nanotechnol. 14 (2023) 262–279, https://doi.org/10.3762/bjnano.14.24.
[32] O. Ohneda, K. Ohneda, F. Arai, J. Lee, T. Miyamoto, Y. Fukushima, D. Dowbenko, L.A. Lasky, T. Suda, ALCAM (CD166): its role in hematopoietic and endothelial development, Blood 98 (7) (2001) 2134–2142, https://doi.org/10.1182/blood.v98.7.2134.
[33] L.T. Senbanjo, M.A. Chellaiah, CD44: a multifunctional cell surface adhesion receptor is a regulator of progression and metastasis of cancer cells, Front. Cell Dev. Biol. 5 (2017) 18, https://doi.org/10.3389/fcell.2017.00018.
[34] A. Gori, R. Frigerio, P. Gagni, J. Burrello, S. Panella, A. Raimondi, G. Bergamaschi, G. Lodigiani, M. Romano, A. Zendrini, A. Radeghieri, L. Barile, M. Cretich, Addressing heterogeneity in direct analysis of extracellular vesicles and their analogs by membrane sensing peptides as pan-vesicular affinity probes, Adv. Sci. 11 (29) (2024) e2400533, https://doi.org/10.1002/advs.202400533.
[35] A. Jha, A.N. Nikam, S. Kulkarni, A. Jha, A.N. Nikam, S. Kulkarni, S.P. Mutalik, A. Pandey, M. Hegde, B.S.S. Rao, S. Mutalik, Biomimetic nanoarchitecturing: a disguised attack on cancer cells, J. Control. Release 329 (2021) 413–433, https://doi.org/10.1016/j.jconrel.2020.12.005.
[36] Y. Zhai, J. Su, W. Ran, P. Zhang, Q. Yin, Z. Zhang, H. Yu, Y. Li, Preparation and application of cell membrane-camouflaged nanoparticles for cancer therapy, Theranostics 7 (10) (2017) 2575–2589, https://doi.org/10.7150/thno.20118.
[37] J. Zhan, D. Zhang, F. Feng, M. Xu, L. Yao, Homotypic and heterotypic adhesion of cancer cells revealed by force-induced remnant magnetization spectroscopy, Nanoscale Horiz. 8 (8) (2023) 1098–1105, https://doi.org/10.1039/d2nh00410k.
[38] H. Yamaguchi, M. Miyazaki, Heterocellular adhesion in cancer invasion and metastasis: interactions between cancer cells and cancer-associated fibroblasts, Cancers 16 (9) (2024) 1636, https://doi.org/10.3390/cancers16091636.
[39] D. Yang, J. Liu, H. Qian, Q. Zhuang, Cancer-associated fibroblasts: from basic science to anticancer therapy, Exp. Mol. Med. 55 (7) (2023) 1322–1332, https://doi.org/10.1038/s12276-023-01013-0.
[40] H. Jia, X. Chen, L. Zhang, M. Chen, Cancer associated fibroblasts in cancer development and therapy, J. Hematol. Oncol. 18 (1) (2025) 36, https://doi.org/10.1186/s13045-025-01688-0.
[41] Y. Chhabra, A.T. Weeraratna, Fibroblasts in cancer: unity in heterogeneity, Cell 186 (8) (2023) 1580–1609, https://doi.org/10.1016/j.cell.2023.03.016.
[42] S. Castorph, et al., Synaptic vesicles studied by SAXS: derivation and validation of a model form factor, J. Phys. Conf. Ser. 247 (2010) 012015, https://doi.org/10.1088/1742-6596/247/1/012015.
[43] M. Cárdenas, et al., Review of structural design guiding the development of lipid nanoparticles for nucleic acid delivery, Curr. Opin. Colloid Interface Sci. 66 (2023) 101705, https://doi.org/10.1016/j.cocis.2023.101705.